Title

EVAP: A two-photon imaging tool to study conformational changes in endogenous Kv2 channels in live tissues

Journal

The Journal of General Physiology, 153(11)

ISSN

0022-1295

Authors

Thapa, Parashar
Stewart, Robert
Sepela, Rebecka J
et al.

Publication Date

2021-11-01

DOI

10.1085/jgp.202012858

Peer reviewed

JGP Journal of General Physiology

ARTICLE

EVAP: A two-photon imaging tool to study conformational changes in endogenous Kv2 channels in live tissues

Parashar Thapa[1*], Robert Stewart[1*], Rebecka J. Sepela[1], Oscar Vivas[2], Laxmi K. Parajuli[2], Mark Lillya[1], Sebastian Fletcher-Taylor[1,3], Bruce E. Cohen[3,4], Karen Zito[2], and Jon T. Sack[1,5*]

A primary goal of molecular physiology is to understand how conformational changes of proteins affect the function of cells, tissues, and organisms. Here, we describe an imaging method for measuring the conformational changes of the voltage sensors of endogenous ion channel proteins within live tissue, without genetic modification. We synthesized GxTX-594, a variant of the peptidyl tarantula toxin guangxitoxin-1E, conjugated to a fluorophore optimal for two-photon excitation imaging through light-scattering tissue. We term this tool EVAP (Endogenous Voltage-sensor Activity Probe). GxTX-594 targets the voltage sensors of Kv2 proteins, which form potassium channels and plasma membrane–endoplasmic reticulum junctions. GxTX-594 dynamically labels Kv2 proteins on cell surfaces in response to voltage stimulation. To interpret dynamic changes in fluorescence intensity, we developed a statistical thermodynamic model that relates the conformational changes of Kv2 voltage sensors to degree of labeling. We used two-photon excitation imaging of rat brain slices to image Kv2 proteins in neurons. We found puncta of GxTX-594 on hippocampal CA1 neurons that responded to voltage stimulation and retain a voltage response roughly similar to heterologously expressed Kv2.1 protein. Our findings show that EVAP imaging methods enable the identification of conformational changes of endogenous Kv2 voltage sensors in tissue.

Introduction

To move the field of voltage-sensitive physiology forward, we need new tools that indicate when and where voltage-sensitive conformational changes in endogenous proteins occur. Many classes of transmembrane proteins have been found to be voltage sensitive (Bezanilla, 2008). One important class of voltage-sensitive proteins is the voltage-gated ion channels. Electrophysiological techniques have enabled remarkably precise studies of the voltage sensitivity of ionic conductances, primarily under reductionist experimental conditions where the channels have been removed from their native tissue. In addition to their canonical function as ion-conducting channels, voltage-gated ion channel proteins have nonconducting functions that are independent of their ion conducting functions (Tanabe et al., 1988; Kaczmarek, 2006). These nonconducting protein functions are largely inaccessible to study by electrophysiology and are more poorly understood. Novel approaches are needed to learn more about voltage sensing in intact tissues and to unlock the mysterious realm of nonconducting voltage-sensitive physiology. Here, we present a new approach to image the conformational changes of endogenous Kv2 voltage-sensitive proteins.

Kv2 proteins form voltage-gated K^+ channels (Frech et al., 1989), bind endoplasmic reticulum proteins to form plasma membrane–endoplasmic reticulum junctions (Johnson et al., 2018; Kirmiz et al., 2018a), regulate a wide variety of physiological responses in tissues throughout the body (Bocksteins, 2016), and integrate their response to voltage with many other cellular processes, including phosphorylation (Murakoshi et al., 1997), SUMOylation (Plant et al., 2011), oxidation (MacDonald et al., 2003), membrane lipid composition (Ramu et al., 2006), and auxiliary subunits (Gordon et al., 2006; Peltola et al., 2011). Kv2 proteins are members of the voltage-gated cation channel superfamily. The voltage sensors of proteins in this superfamily comprise a bundle of four transmembrane helices termed S1–S4 (Long et al., 2005, 2007). The S4 helix contains positively charged arginine and lysine residues, gating charges, that respond to voltage changes by moving through the transmembrane electric field (Aggarwal and MacKinnon, 1996; Seoh et al.,

[1]Department of Physiology and Membrane Biology, University of California, Davis, Davis, CA; [2]Center for Neuroscience, University of California, Davis, Davis, CA; [3]The Molecular Foundry, Lawrence Berkeley National Laboratory, Berkeley, CA; [4]Division of Molecular Biophysics and Integrated Bioimaging, Lawrence Berkeley National Laboratory, Berkeley, CA; [5]Department of Anesthesiology and Pain Medicine, University of California, Davis, Davis, CA.

*P. Thapa and R. Stewart contributed equally to this paper; Correspondence to Jon T. Sack: jsack@ucdavis.edu.

1996; Islas and Sigworth, 1999). When voltage sensor domains encounter a transmembrane voltage that is more negative on the inside of the cell membrane, voltage sensors are biased toward resting conformations, or down states, in which gating charges are localized intracellularly. When voltage becomes more positive, gating charges translate toward the extracellular side of the membrane, and voltage sensors are progressively biased toward up states in a process of voltage activation (Armstrong and Bezanilla, 1973; Zagotta et al., 1994; Tao et al., 2010; Xu et al., 2019). Channel pore opening is distinct from, but coupled to, voltage sensor movement. In some voltage-gated ion channel proteins, voltage sensor movement is coupled to nonconducting protein functions (Tanabe et al., 1988; Kaczmarek, 2006). To study the functional outputs of voltage sensors, it is essential to measure voltage sensor activation itself. Conformational changes of voltage sensors have been detected with electrophysiological measurements of gating currents (Armstrong and Bezanilla, 1973; Schneider and Chandler, 1973; Bezanilla, 2018) or by optical measurements from fluorophores inserted near voltage sensors by genetic encoding (Lin and Schnitzer, 2016) or chemical modification (Zhang et al., 2015). However, the following experimental limitations prevent these existing techniques from measuring conformational changes of voltage sensors of most endogenous proteins: gating currents can only be measured when the proteins are expressed at high density in a voltage-clamped membrane; engineered proteins differ from endogenous channels; most chemical modification strategies result in off-target labeling; and conjugation of fluorophores into voltage sensors irreversibly alters structure and function. Here, we develop a different strategy to reveal conformational states of Kv2 proteins.

To image where in tissue the voltage sensors of Kv2 proteins adopt a specific resting conformation, we exploited the conformation-selective binding of the tarantula peptide guangxitoxin (GxTX)-1E, which can be conjugated to fluorophores to report Kv2 conformational changes (Tilley et al., 2014; Fletcher-Taylor et al., 2020; Stewart et al., 2021). Here, we synthesize GxTX-594, a Ser13Cys GxTX variant conjugated to Alexa Fluor 594, a fluorophore compatible with two-photon excitation imaging through light-scattering tissue. GxTX-594 dynamically binds Kv2 channels in living tissue. When GxTX-594 binds, it becomes immobilized and fluorescently labels Kv2 proteins at the cell surface. When Kv2 channels become voltage activated, GxTX-594 unbinds, resulting in unlabeling (see illustration). This labeling/unlabeling dynamic is similar to a recently reported point accumulation for imaging of nanoscale topology superresoluton imaging method (Legant et al., 2016), yet the method reported here is sensitive to changes in protein conformation. GxTX-594 labeling of Kv2 proteins equilibrates on the time scale of seconds, revealing the probability (averaged over time) that unbound voltage sensors are resting or active. Here, we develop a method to calculate the average conformational status of unlabeled Kv2 proteins from images of GxTX-594 fluorescence and deploy the GxTX-594 probe in brain slices to image voltage-sensitive fluorescence changes that reveal conformational changes of endogenous neuronal Kv2 proteins. We refer to this type of imaging tool as an Endogenous Voltage-sensor Activity Probe (EVAP). This EVAP approach provides an imaging technique to study conformational changes of endogenous voltage-sensitive Kv2 proteins in samples that have not (or cannot) be genetically modified.

Materials and methods

GxTX-594 synthesis

We used solid-phase peptide synthesis to generate a variant of GxTX, an amphiphilic 36-amino acid cystine knot peptide. We synthesized the same peptide used for GxTX-550, Ser13Cys GxTX, where a free thiolate side chain of cysteine 13 is predicted to extend into extracellular solution when the peptide is bound to a voltage sensor (Tilley et al., 2014). GxTX-1E folds by formation of three internal disulfides, and cysteine 13 was differentially protected during oxidative refolding to direct chemoselective conjugation. Following refolding and thiol deprotection, Alexa Fluor 594 C_5 maleimide was condensed with the free thiol, and Ser13Cys (Alexa Fluor 594) GxTX-1E (called GxTX-594) was purified (Fig. S1).

The Ser13Cys GxTX peptide was synthesized as previously described (Tilley et al., 2014). Methionine 35 of GxTX was replaced by the oxidation-resistant noncanonical amino acid norleucine to avoid complications from methionine oxidation, and serine 13 was replaced with cysteine to create a spinster thiol. Ser13Cys GxTX was labeled with a Texas Red derivative (Alexa Fluor 594 C_5 maleimide, cat. #10256; Thermo Fisher Scientific) to form GxTX-594. Ser13Cys GxTX lyophilisate was brought to 560 µM in 50% acetonitrile (ACN) + 1 mM Na_2EDTA. 2.4 µl of 1M Tris (pH 6.8 with HCl), 4 µl of 10 mM Alexa Fluor 594 C_5 maleimide in DMSO, and 17.9 µl of 560 µM Ser13Cys GxTX were added for a final solution of 100 mM Tris, 1.6 mM Alexa Fluor 594 C_5 maleimide, and 0.4 mM GxTX in 24 µl of reaction solution. Reactants were combined in a 1.5-ml low-protein–binding polypropylene tube (LoBind, cat. #022431081; Eppendorf) and mixed at 1,000 rpm at 20°C for 4 h (Thermomixer 5355 R; Eppendorf). After incubation, the tube was centrifuged at 845 RCF for 10 min at room temperature. A purple pellet was observed after centrifugation. The supernatant was transferred to a fresh tube and centrifuged at 845 RCF for 10 min. After this second centrifugation, no visible pellet was seen. The supernatant was injected onto a reverse-phase HPLC C_{18} column (Biobasic 4.6-mm RP-C_{18} 5 µm, cat. #2105-154630; Thermo Fisher Scientific) equilibrated in 20% ACN, 0.1% trifluoroacetic acid (TFA) at 1 ml/min, and eluted with a protocol holding in 20% ACN for 2 min, increasing to 30% ACN over 1 min, then increasing ACN at 0.31% per minute. HPLC effluent was monitored by fluorescence and an absorbance array detector. 1-ml fractions were pooled based on fluorescence (280-nm

excitation, 350-nm emission) and absorbance (214 nm, 280 nm, and 594 nm). GxTX-594 peptide–fluorophore conjugate eluted at ∼35% ACN, and mass was confirmed by mass spectrometry using a Bruker ultrafleXtreme matrix-assisted laser desorption ionization time-of-flight (MALDI-TOF; Fig. S1). Samples for identification from HPLC eluant were mixed 1:1 in an aqueous solution of 25% MeOH and 0.05% TFA saturated with α-cyano-4-hydrocinnamic acid, pipetted onto a ground-steel plate, dried under vacuum, and ionized with 60–80% laser power. Molecular species were detected using a reflector mode protocol and quantitated using Bruker Daltonics flexAnalysis 3.4 software. Lyophilizate containing GxTX-594 conjugation product was dissolved in cell external (CE) buffer (defined below) and stored at −80°C. GxTX-594 concentration was determined by 280-nm absorbance using a calculated molar attenuation coefficient of 18,900 M^{-1} cm^{-1}.

Chinese hamster ovary (CHO) cell methods

CHO cell culture and transfection

The CHO-K1 cell line (American Type Culture Collection) and a subclone transfected with a tetracycline-inducible rat Kv2.1 construct (Kv2.1-CHO; Trapani and Korn, 2003) were cultured as described previously (Tilley et al., 2014). To induce Kv2.1 expression in Kv2.1-TREx-CHO cells, 1 µg/ml minocycline (cat. #ALX-380-109-M050; Enzo Life Sciences), prepared in 70% ethanol at 2 mg/ml, was added to the maintenance media to induce Kv2.1 expression. Minocycline was added 40–48 h before imaging and voltage-clamp fluorometry experiments. Minocycline was added 1–2 h before whole-cell ionic current recordings to limit K^+ conductance such that voltage clamp could be maintained. Transfections were achieved with Lipofectamine 2000 (cat. #1668027; Life Technologies). 1.1 µl Lipofectamine was diluted, mixed, and incubated in 110 µl of Opti-MEM (product no. 31985062, lot no. 1917064; Gibco-BRL) in a 1:100 ratio for 5 min at room temperature. Concurrently, 1 µg of plasmid DNA and 110 µl of Opti-MEM were mixed in the same fashion. DNA and Lipofectamine 2000 mixtures were mixed and left at room temperature for 20 min. Then, the transfection cocktail mixture was added to 2 ml of culture media in a 35-mm cell culture dish of CHO cells at ∼40% confluency and allowed to settle at 37°C in 5% CO_2 for 4–6 h before the media were replaced. Cells were given 40–48 h recovery following transfection before being used for experiments. Rat Kv2.1-GFP (Antonucci et al., 2001), rat Kv2.2-GFP (Kirmiz et al., 2018b), rat Kv1.5-GFP (Li et al., 2001), rat Kv4.2-GFP (Shibata et al., 2003), mouse BK-GFP, rat KvBeta2 (Shibata et al., 2003), and rat KCHiP2 (An et al., 2000) plasmids were all gifts from James Trimmer (University of California, Davis, Davis, CA). Identities of constructs were confirmed by sequencing from their cytomegalovirus promoter. To minimize any day-to-day variances, the cells in experiments shown in Fig. 4 or Fig. S2 were each plated for all transfections from a single-cell suspension, transfected in parallel, and imaged 2 d later using the same thawed aliquot of GxTX-594.

Confocal and Airy disk imaging

Confocal images were obtained with an inverted confocal system (LSM 880 410900-247-075; Zeiss) run by ZEN Black 2.1 software. A 63×/1.40 NA oil DIC objective (420782-9900-799; Zeiss) was used for most imaging experiments; a 63×/1.2 NA water DIC objective (441777-9970-000; Zeiss) was used for voltage clamp fluorometry experiments. GFP and YFP were excited with the 488-nm line from an argon laser (3.2 mW at installation) powered at 0.5% unless otherwise noted. GxTX-594 was excited with a 594-nm helium–neon laser (0.6 mW at installation) powered at 10% unless otherwise noted. Wheat germ agglutinin (WGA)-405 was excited with a 405-nm diode laser (3.5 mW at installation) powered at 1% unless otherwise noted. Temperature inside the microscope housing was 27–30°C.

In confocal imaging mode, fluorescence was collected with the microscope's 32-detector gallium arsenide phosphide detector array arranged with a diffraction grating to measure 400–700-nm emissions in 9.6-nm bins. Emission bands were 495–550 nm for GFP and YFP, 605–700 nm for GxTX-594, and 420–480 nm for WGA-405. Point spread functions were calculated using ZEN Black software using emissions from 0.1-µm fluorescent microspheres prepared on a slide according to manufacturer's instructions (cat. #T7279; Thermo Fisher Scientific). The point spread functions for confocal images with the 63×/1.40 NA oil DIC objective in the x–y direction were 228 nm (488-nm excitation) and 316 nm (594-nm excitation).

In Airy disk imaging mode, fluorescence was collected with the microscope's 32-detector gallium arsenide phosphide detector array arranged in a concentric hexagonal pattern (Airyscan 410900-2058-580; Zeiss). After deconvolution, the point spread functions for the 63×/1.40 NA oil objective with 488-nm excitation was 124 nm in x–y and 216 nm in z and with 594-nm excitation, 168 nm in x–y and 212 nm in z. For the 63×/1.2 NA water objective, the point spread function with 488-nm excitation was 187 nm in x–y and 214 nm in z and with 594-nm excitation, 210 nm in x–y and 213 nm in z.

Unless stated otherwise, cells were plated in uncoated 35-mm dishes with a 7-mm inset no. 1.5 coverslip (cat. #P35G-1.5-20-C; MatTek). The CHO CE solution used for imaging and electrophysiology contained (in mM): 3.5 KCl, 155 NaCl, 10 HEPES, 1.5 $CaCl_2$, and 1 $MgCl_2$, adjusted to pH 7.4 with NaOH. Measured osmolality was 315 mOsm/liter. When noted, solution was supplemented with either 10 mM glucose (CEG) or 10 mM glucose and 1% BSA (CEGB).

For time lapse, GxTX-594 concentration–effect experiments, Kv2.1-CHO cells were plated onto 22 × 22-mm no. 1.5H coverglass (Deckglaser), and Kv2.1 expression was induced with minocycline 48 h before experiments such that all Kv2.1-CHO cells expressed Kv2.1. Prior to imaging, cell maintenance media were removed and replaced with CEGB, then the coverslip was mounted on an imaging chamber (cat. #RC-24E; Warner Instruments) with vacuum grease. We performed three 10-fold serial dilutions of 1,000 nM GxTX-594 to generate the range of concentrations used for this concentration–effect experiment and applied each concentration of GxTX-594 to Kv2.1-CHO cells for 15 min followed by 15 min of washout before the next concentration of GxTX-594 was applied. Solutions were added to the imaging chamber perfusion via a syringe at a flow rate of ∼1 ml per 10 s. Images were taken every 5 s. Laser power was set to 0.5% for the 488-nm laser and 1.5% for the 594-nm laser. For

colocalization experiments with GFP-tagged proteins, cells were incubated in 100 nM GxTX-594 for 5 min and then washed with 1 ml CEGB three times before imaging.

Whole-cell voltage clamp for CHO cell imaging

Kv2.1-CHO cells plated in glass-bottom 35-mm dishes were incubated in minocycline for 48 h to induce Kv2.1 channel expression. Cells were washed with CEGB, placed in the microscope, and then incubated in 100 µl of 100 nM GxTX-594 for 5 min to label cells. Before patch clamp, the solution was diluted with 1 ml of CEG for a working concentration of 9 nM GxTX-594 during experiments. We determined the time required for GxTX-594 to reach a stable fluorescence after dilution from 100 nM to 9 nM by time-lapse imaging during dilution (Fig. 5 A). The rate of fluorescence change ($k_{\Delta F}$) indicated that, on average, equilibration was 85% complete 9 min after dilution to 9 nM. After dilution to 9 nM, the mean fluorescence intensity decreased by 39.1 ± 8.4% and remained stable (Fig. 5 B). Cells with obvious GxTX-594 surface staining were voltage clamped in whole-cell mode with an EPC-10 patch-clamp amplifier (HEKA Elektronik) run by Patchmaster software (v2 × 90.2; HEKA Elektronik). The patch pipette contained the following potassium-deficient Cs^+ internal pipette solution to reduce voltage error by limiting outward current: 70 mM CsCl, 50 mM CsF, 35 mM NaCl, 1 mM EGTA, and 10 mM HEPES, brought to pH 7.4 with CsOH. Osmolality was 310 mOsm/liter. The liquid junction potential was calculated to be 3.5 mV and was not corrected. Borosilicate glass pipettes (cat. #BF150-110-10HP; Sutter Instruments) were pulled with blunt tips to resistances <3.0 MΩ in these solutions. Cells were held at −80 mV (unless noted otherwise) and stepped to indicated voltages. The voltage step stimulus was maintained until any observed change in fluorescence was complete. Cells were stepped to −80 mV for at least 1 min and were visually inspected to determine sufficient fluorescence recovery before being stepped to another voltage. This recovery time did not always allow GxTX-594 labeling to equilibrate fully. For stimulus frequency dependence experiments, cells were given 2-ms steps to 40 mV at the stated frequencies (0.02, 5, 10, 20, 50, 100, 150, or 200 Hz). Images for voltage clamp fluorometry were taken in Airy disk imaging mode with the settings described above.

During time-lapse imaging of voltage-clamped cells, we noticed that GxTX-594 fluorescence in the center of the glass-adhered surface responded more slowly to voltage changes than the periphery. At −80 mV, at the center of the glass-adhered cell surface, relabeling was incomplete after 500 s; however, at the cell periphery, relabeling neared completion within 200 s (Fig. S4 A). To quantify this observation, concentric circular regions of interest (ROIs) were drawn, with the smallest ROI in the center of the glass-adhered surface. The average fluorescence intensities from each of these ROIs were compared with each other and an ROI at the cell periphery (Fig. S4, B and C). We quantified $k_{\Delta F}$ by fitting the average fluorescence intensities from each ROI with a monoexponential function (Eq. 1 in Image analysis). In response to voltage change, the $k_{\Delta F}$ was consistently slower at the center of the glass-adhered surface and faster toward the outer periphery (Fig. S4, D and E). While $k_{\Delta F}$ was consistently slower at the center of the glass-adhered surface, we observed that $k_{\Delta F}$ was more pronounced during labeling at −80 mV than unlabeling at 40 mV. When cells were held at a membrane potential of −80 mV, $k_{\Delta F}$ at the periphery was ∼10-fold faster than the $k_{\Delta F}$ at the center of the cell. In comparison, when the membrane potential was held at 40 mV, $k_{\Delta F}$ at the periphery was approximately threefold faster than the $k_{\Delta F}$ at the center of the cell. The gradual change in fluorescence intensity over many seconds after a voltage step is inconsistent with a fast electrochromic effect leading to fluorescence change as the change in fluorescence intensity does not occur instantaneously when the membrane potential is stepped. Additionally, the slowing of $k_{\Delta F}$ in subcellular regions farther from the periphery of cells is inconsistent with a slower electrochromic effect as whole-cell voltage clamp should render the membrane surface isopotential.

K^+ channel–GFP ionic current recordings

Whole-cell voltage clamp was used to measure currents from CHO cells expressing Kv2.1-GFP, Kv2.2-GFP, Kv1.5-GFP, Kv4.2-GFP, BK-GFP, or GFP that was transfected as described above. Cells were plated on glass-bottom dishes. Cells were held at −80 mV, then 100-ms voltage steps were delivered ranging from −80 mV to +80 mV in +5-mV increments. Pulses were repeated every 2 s. The external (bath) solution contained CE solution. The internal (pipette) solution contained (in mM) 35 KOH, 70 KCl, 50 KF, 50 HEPES, and 5 EGTA, adjusted to pH 7.2 with KOH. Liquid junction potential was calculated to be 7.8 mV and was not corrected. Borosilicate glass pipettes (cat. #BF150-110-10HP; Sutter Instruments) were pulled into pipettes with resistance <3 MΩ for patch clamp recording. Recordings were at room temperature (22–24°C). Voltage clamp was achieved with an Axon Axopatch 200B Amplifier (Molecular Devices) run by Patchmaster software (v2 × 90.2; HEKA Elektronik). Holding potential was −80 mV capacitance and ohmic leak were subtracted using a P/5 protocol. Recordings were low-pass filtered at 10 kHz and digitized at 100 kHz. Voltage clamp data were plotted with Igor Pro 7 (WaveMetrics). As the experiments plotted in Fig. S2 A were merely to confirm functional expression of ion channels at the cell surface, series resistance compensation was not used, and substantial cell voltage errors are predicted during these experiments.

Kv2.1 ionic current recordings

Prior to patching, Kv2.1-CHO cells were washed in divalent-free PBS and then harvested in Versene (cat. #15040066; Gibco-BRL). Cells were scraped and transferred to a polypropylene tube, pelleted, and washed three times at 1,000 *g* for 2 min and then resuspended in the same external solution as used in the recording chamber bath. Cells were rotated in a polypropylene tube at room temperature (22–24°C) until use. Cells were then pipetted into a 50-µl recording chamber (RC-24N; Warner Instruments) prefilled with external solution and allowed to settle for ≥5 min. After adhering to the bottom of the glass recording chamber, cells were thoroughly rinsed with external solution using a gravity-driven perfusion system. Cells showing uniform intracellular GFP expression of intermediate intensity were selected for patching.

Voltage clamp was achieved with a patch clamp amplifier (Axon Axopatch 200B; Molecular Devices) run by Patchmaster software. Borosilicate glass pipettes (BF150-110-7.5HP; Sutter Instruments) were pulled with blunt tips, coated with silicone elastomer (Sylgard 184; Dow Corning), heat cured, and tip fire-polished to resistances <4 MΩ. Capacitance and ohmic leak were subtracted using a P/5 protocol. Recordings were low-pass filtered at 10 kHz using the amplifier's built-in Bessel function and digitized at 100 kHz.

For whole-cell ionic current measurements in Kv2.1-CHO cells, the external patching solution contained (in mM) 3.5 KCl, 155 NaCl, 10 HEPES, 1.5 $CaCl_2$, and 1 $MgCl_2$, adjusted to pH 7.4 with NaOH. The internal (pipette) solution contained (in mM) 70 KCl, 5 EGTA, 50 HEPES, 50 KF, and 35 KOH, adjusted to pH 7.4 with KOH. The osmolality was 315 mOsm/liter for the external solution and 310 mOsm/liter for the internal solution measured by a vapor pressure osmometer. Following establishment of the whole-cell seal, ionic K^+ current recordings were taken in the presence of a vehicle, which consisted of 100 nM tetrodotoxin, 10 mM glucose, and 0.1% BSA prepared in external solution. Cells were held at −100 mV with channel activation steps ranging from −80 mV to +120 mV in increments of +5 mV (100 ms) before being returned to 0 mV (100 ms) to record tail currents. The intersweep interval was 2 s. To determine the bioactivity of GxTX-594, Kv2.1 ionic currents were recorded once more, 5 min following the wash-in of bath solution also containing 100 nM GxTX-594. Wash-ins were performed while holding at −100 mV; 100 µl was washed through the chamber and removed distally through vacuum tubing to maintain constant bath fluid level.

Ionic current analysis

The average current in the 100 ms before voltage step was used to zero subtract the recording. Outward current taken as the mean value between 90 and 100 ms of the channel activation step was used to calculate and correct for series resistance-induced voltage error. Tail current values were derived from the mean value between 0.2 and 1.2 ms of the 0-mV tail current step. Tail current was normalized by the mean activation step current from 50 to 80 mV and plotted against the estimated membrane potential, which had been corrected for voltage error and the calculated liquid junction potential of 8.5 mV. These tail *GV* plots were fit with a fourth-power Boltzmann function (Sack et al., 2004), and the fit parameters were used for statistical analysis.

Brain slice methods

Hippocampal slice culture preparation and transfection

All experimental procedures were approved by the University of California, Davis, institutional animal care and use committee and were performed in strict accordance with the Guide for the Care and Use of Laboratory Animals of the National Institutes of Health. Animals were maintained under standard light–dark cycles and had ad libitum access to food and water. Organotypic hippocampal slice cultures were prepared from postnatal day 5–7 rats, as previously described (Stoppini et al., 1991) and detailed in a video protocol (Opitz-Araya and Barria, 2011). DIV15–30 neurons were transfected 2–6 d before imaging via biolistic gene transfer (160 psi, Helios gene gun; Bio-Rad) as described in a detailed video protocol (Woods and Zito, 2008). 10 µg of plasmid was coated to 6–8 mg of 1.6-µm gold beads.

Two-photon excitation slice imaging

Image stacks (512 × 512 pixels, 1-mm Z-steps, 0.035 µm/pixel) were acquired using a custom two-photon excitation microscope (LUMPLFLN 60XW/IR2 objective, 60×/1.0 NA; Olympus) with two pulsed Ti:sapphire lasers (Mai Tai; Spectra Physics) tuned to 810 nm (for GxTX-594 imaging) and 930 nm (for GFP imaging) and controlled with ScanImage software (Pologruto et al., 2003). After identifying a neuron expressing Kv2.1-GFP, perfusion was stopped, and GxTX-594 was added to the static bath solution to a final concentration of 100 nM. After 5-min incubation, perfusion was restarted, leading to washout of GxTX-594 from the slice bath. Red and green photons (565dcxr, BG-22 glass, HQ607/45; Chroma Technology) emitted from the sample were collected with two sets of photomultiplier tubes (R3896; Hamamatsu).

Whole-cell voltage clamp for brain slice imaging

Organotypic hippocampal slice cultures (6–7 DIV, not transfected) were transferred to an imaging chamber with recirculating artificial cerebrospinal fluid (ACSF) maintained at 30°C. To hold the slice to the bottom of the chamber, a horseshoe-shaped piece of gold wire was used to weight the membrane holding the slice. ACSF contained (in mM) 127 NaCl, 25 $NaHCO_3$, 25 D-glucose, 2.5 KCl, 1.25 NaH_2PO_4, 1 $MgCl_2$, 2 $CaCl_2$, and 200 nM tetrodotoxin, pH 7.3, and aerated with 95% O_2/5% CO_2 (~310 mOsm). 4 ml of 100 nM GxTX-594 in ACSF was used in the circulating bath to allow the toxin to reach the slice and reach the desired concentration of 100 nM throughout the circulating bath. Images were acquired beginning 3 min after GxTX-594 was added. Apparent CA1 neurons with GxTX-594 labeling in a Kv2-like pattern were selected for whole-cell patch clamp. Voltage clamp was achieved using an Axopatch 200B Amplifier (Molecular Devices) controlled with custom software written in MATLAB (MathWorks, Inc.). Patch pipettes (5–7 MΩ) were filled with intracellular solution containing (in mM) 135 Cs-methanesulfonate, 10 Na_2-phosphocreatine, 3 Na-L-ascorbate, 4 NaCl, 10 HEPES, 4 $MgCl_2$, 4 Na_2ATP, and 0.4 NaGTP, pH 7.2. Neurons were clamped at −70 mV. Input resistance and holding current were monitored throughout the experiment. Cells were excluded if the pipette series resistance was >25 MΩ or if the holding current exceeded −100 pA. To activate Kv2 channels, a 50-s depolarizing step from −70 mV to 0 mV was given.

Image analysis

Fluorescence images were analyzed using ImageJ 1.52n software (Schneider et al., 2012). ROIs encompassed the entire fluorescent region of an individual cell or neuron unless mentioned otherwise. ROIs were drawn manually. Analysis of images was conducted independently by multiple researchers who produced similar results, but analysis was not conducted in a blinded or randomized fashion. Fluorescence intensity (*F*) was background subtracted using the mean *F* of a region that did not contain cells. In experiments with CHO cells where the bath solution contained 9 nM GxTX-594, the apparent surface membrane of most cells (40

of 47) lacking Kv2.1-GFP protein had lower F than the background region that did not contain cells (Fig. S3 B, horizontal black dashed line), indicating that the background F was overestimated. Based on the mean F from the apparent surface membrane of cells lacking Kv2.1 protein, the background was overestimated by 24%. The signal from the surface membrane of cells stably transfected with rat Kv2.1 (Kv2.1-CHO) was, on average, 18× higher than regions that did not contain cells, making the error generated by our overestimation of the background ∼1%. As the error produced by this background subtraction method was relatively small, it was not corrected. For F/F_{init} normalization, F_{init} was the mean fluorescence preceding the indicated voltage stimuli, or the max observed intensity in concentration–effect experiments. Further details of specific normalization and background subtraction procedures are provided in the figure legends. Time dependence of fluorescence intensity was fit with a monoexponential decay:

$$F = F_\infty + (F_0 - F_\infty)\, e^{-\frac{(t-t_0)}{\tau}}, \tag{1}$$

where $\tau = 1/k_{\Delta F}$, t = time, t_0 = time at start of fit, F = fluorescence intensity, F_0 = fluorescence at start of fit, and F_∞ = fluorescence after infinite time.

The Kv2.1–GxTX-594, fluorescence–voltage (FV) responses were fit with a Boltzmann function:

$$f(V) = \mathit{offset} + A\left\{\frac{1}{1 + e^{-\left[\left(V - V_{\frac{1}{2}}\right)*\frac{zF}{RT}\right]}}\right\}, \tag{2}$$

where V = voltage, offset = the offset from zero of the Boltzmann distribution, A = the amplitude, z = number of elementary charges, F = Faraday's constant, R = the universal gas constant, and T = temperature (held at 295°K).

For colocalization analyses, the Pearson coefficient was calculated using the JACoP plugin (Bolte and Cordelières, 2006). Colocalization analyses were conducted within ROIs defining individual cells. A Pearson correlation coefficient value of 0 signifies uncorrelated pixels between two images, and a Pearson correlation coefficient value of 1 signifies complete correlation between pixels from two images. Correlation between pixels from two fluorescent recordings of an image suggests spatial colocalization of proteins. Plotting and curve fitting was performed with Igor Pro 7 or 8 (WaveMetrics), which performs nonlinear least squares fits using a Levenberg–Marquardt algorithm. Sample sizes of $n \geq 3$ were selected to confirm reproducibility. Sample sizes of $n \geq 6$ were selected to power nonparametric statistical comparisons to discern $P < 0.01$. The α for statistical significance in nonparametric statistical comparisons was adjusted for multiple comparisons using the Bonferroni method. The Bonferroni-corrected P value = $\frac{\alpha}{n}$, where $\alpha = 0.01$ and n represents the number of comparisons made in an experiment. Error values from individual curve fittings are SDs. All other errors, including error bars, indicate SEs. Arithmetic means are reported for intensity measurements and correlation coefficients. As the distributions underlying variability in results are unknown, nonparametric statistical comparisons were conducted with Mann–Whitney U tests, and two-tailed P values were reported individually if $P > 0.0001$. Parametric statistical tests, which include the Student's t test, ANOVA, and Tukey's post hoc test, were performed with paired data and on sample sizes of $n \leq 6$ due to the weak statistical power of nonparametric tests when comparing small sample sizes.

EVAP model

In the EVAP model, at any given voltage, there is a probability that a voltage sensor is either in its resting conformation ($P_{resting}$) or in its activated conformation ($P_{activated}$) such that $P_{activated} = (1 - P_{resting})$. The equilibrium for voltage sensor activation is then a ratio of activated-to-resting voltage sensors ($P_{activated}/P_{resting}$) in which

$$\frac{P_{activated}}{P_{resting}}\, unlabeled = e^{(V - V_{1/2,unlabeled})\frac{zF}{RT}} \tag{3a}$$

$$\frac{P_{activated}}{P_{resting}}\, labeled = e^{(V - V_{1/2,labeled})\frac{zF}{RT}}, \tag{3b}$$

where $V_{1/2}$ is the voltage where $P_{activated}/P_{resting} = 1$. In a prior study, our analysis of the conductance–voltage relation of Kv2.1 yielded a $V_{1/2} = -32$ mV with $z = 1.5$ elementary charges (e_0) for the early movement of four independent voltage sensors, and we found that with a saturating concentration of GxTX, the $V_{1/2}$ = +42 mV (Fig. 1 C; Tilley et al., 2019). These values were used for $V_{1/2,unlabeled}$, z, and $V_{1/2,labeled}$, respectively (Table 1). To relate voltage sensor activation to transient labeling and unlabeling, we used microscopic binding ($k_{on}[EVAP]$) and unbinding (k_{off}) rates that are distinct for resting and activated voltage sensors. We estimated values for these rates assuming

$$k_{\Delta F} = k_{on}[EVAP] + k_{off} \tag{4}$$

and

$$K_d = \frac{k_{off}}{k_{on}}. \tag{5}$$

To calculate the $k_{on,resting}$ and $k_{off,resting}$ values reported in Table 1, we used the saturating value at negative voltages of the $k_{\Delta F}$–voltage relation (see Fig. 6 E), and K_d from concentration–effect imaging (Fig. 2 D). In 9 nM GxTX-594, at greater than +40 mV, voltage-dependent unlabeling was nearly complete, indicating that $k_{off,activated} >> k_{on,activated}[EVAP]$. The model does not include EVAP signal that is insensitive to voltage (Fig. 6 C). We input the saturating amplitude of the Boltzmann fit to the $k_{\Delta F}$ at positive voltages as $k_{off,activated}$ (Fig. 6 E). The slow labeling of activated voltage sensors confounded attempts to measure $k_{on,activated}$ directly, and we used the statistical thermodynamic principle of microscopic reversibility (Lewis, 1925) to constrain $k_{on,activated}$:

$$\frac{\frac{P_{activated}}{P_{resting}}, labeled}{\frac{P_{activated}}{P_{resting}}, unlabeled} = \frac{\frac{k_{off,resting}}{k_{on,resting}}}{\frac{k_{off,activated}}{k_{on,activated}}}. \tag{6}$$

The EVAP model depicted in Scheme 2 has only a single microscopic binding rate, $k_{on,total}[EVAP]$, and unbinding rate, $k_{off,total}$. $k_{on,total}$ is a weighted sum of both $k_{on,resting}$ and $k_{on,activated}$ from Scheme 1. The weights for $k_{on,total}$ are the relative probabilities that unlabeled voltage sensors are resting or activated, which is determined at any static voltage by an equilibrium constant, $\frac{P_{activated}}{P_{resting}}\, unlabeled$:

$$k_{on,total} = k_{on,resting}[EVAP] \cdot \frac{1}{1 + \frac{P_{activated}}{P_{resting}} unlabeled} + k_{on,active}[EVAP] \cdot \frac{1}{1 + \frac{1}{\frac{P_{activated}}{P_{resting}} unlabeled}}. \quad (7)$$

Similarly, $k_{off,total}$ is determined by the unbinding rate from resting voltage sensors ($k_{off,resting}$) and the unbinding rate from activated voltage sensors ($k_{off,activated}$) and weighted such that

$$k_{off,total} = k_{off,resting} \cdot \frac{1}{1 + \frac{P_{activated}}{P_{resting}} labeled} + k_{off,active} \cdot \frac{1}{1 + \frac{1}{\frac{P_{activated}}{P_{resting}} labeled}}. \quad (8)$$

Using $k_{on,total}$ and $k_{off,total}$, we compute $k_{\Delta F}$ using Eq. 4, as implemented in Data S1.

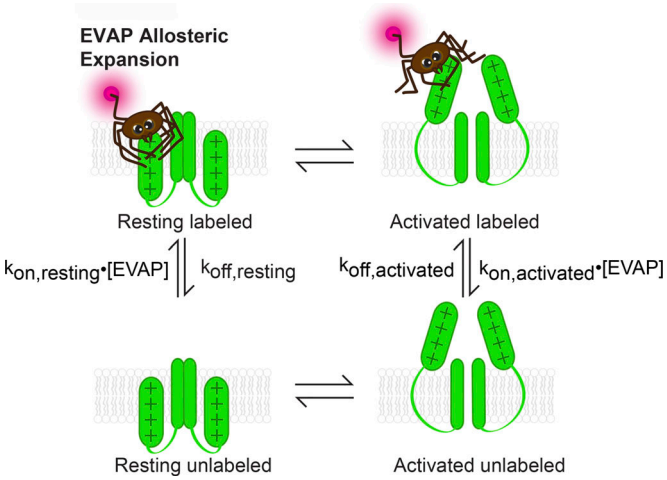

(Scheme 1)

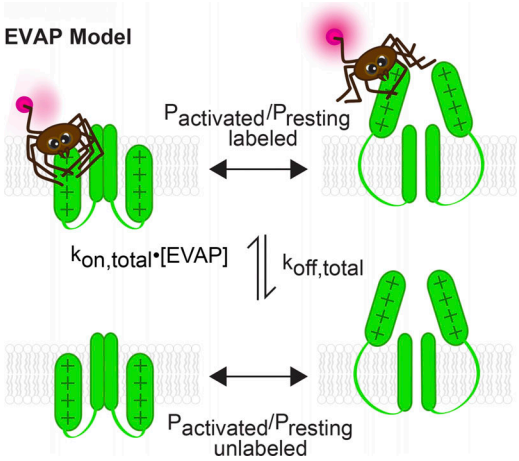

(Scheme 2)

The EVAP model was also used to predict the magnitude of GxTX-594 fluorescence changes on cell surfaces. In theory, the ratio of fluorescence at a test voltage to fluorescence at a prior voltage (F/F_{init}) is equal to the probability that a Kv2 subunit is reversibly labeled by GxTX-594 ($P_{labeled}$):

$$\frac{F}{F_{init}} = \frac{P_{labeled}}{P_{labeled,init}}. \quad (9)$$

The equilibrium $P_{labeled}$ at any voltage can be determined from microscopic binding rates associated with Scheme 2 where

$$P_{labeled} = \frac{1}{1 + \frac{K_{d,total}}{[EVAP]}} = \frac{1}{1 + \frac{k_{off,total}}{k_{on,total} \cdot [EVAP]}}. \quad (10)$$

Predictions of F / F_{init} and $k_{\Delta F}$ during trains of 2-ms voltage steps from −80 mV to +40 mV were made from the EVAP model by summing the products of time-averaged probability of being at each voltage (P_{Vn}) and the fluorescence change predicted at that voltage (ΔF_{Vn}) :

$$F/F_{init} = (P_{V1} \cdot \Delta F_{V1}) + (P_{V2} \cdot \Delta F_{V2}) + \ldots + (P_{Vn} \cdot \Delta F_{Vn}). \quad (11)$$

For voltage steps from −80 to +40 mV, Eq. 11 is:

$$F/F_{init} = (P_{40mV} \cdot \Delta F_{40mV}) + (P_{-80mV} \cdot \Delta F_{-80mV}).$$

We predicted EVAP kinetic responses as

$$k_{\Delta F} = (P_{V1} \cdot k_{\Delta F,V1}) + (P_{V2} \cdot k_{\Delta F,V2}) + \ldots + (P_{Vn} \cdot k_{\Delta F,Vn}), \quad (12)$$

where P_{Vn} is as in Eq. 11 and $k_{\Delta F,n}$ is $k_{\Delta F}$ at that particular voltage. For voltage steps from −80 to +40 mV, Eq. 12 is:

$$k_{\Delta F} = (P_{40mV} \cdot k_{\Delta F40mV}) + (P_{-80mV} \cdot k_{\Delta F-80mV}).$$

Online supplemental material

Fig. S1 pertains to the synthesis of GxTX-594. It shows a model of GxTX-594, and provides HPLC chromatograms and MALDI-TOF mass spectrometry profiles of Ser13Cys GxTX and GxTX-594. Fig. S2 shows GxTX-594 selectively labeling Kv2 proteins at the cell surfaces. Fig. S3 shows that GxTX-594 labeling of surface membranes requires Kv2 proteins. Fig. S4 demonstrates that extracellular access can impact GxTX-594 labeling kinetics. Fig. S5 demonstrates that variation in bath temperature does not account for variability of GxTX-594 kinetics. Fig. S6 is an extended image gallery of GxTX-594 labeling CA1 hippocampal pyramidal neurons transfected with Kv2.1 GFP. Video 1 is a time-lapse image sequence of GxTX-594 fluorescence on a voltage-clamped CA1 hippocampal pyramidal neuron while it is depolarized from −70 to 0 mV. Data S1 is a spreadsheet that sets up calculations to generate EVAP model predictions.

Results

GxTX-594 retains bioactivity for Kv2.1 after chemoselective modification

To monitor activation of Kv2 proteins in tissue slices, we synthesized an EVAP compatible with two-photon imaging. We previously presented an EVAP that was a synthetic derivative of GxTX conjugated to a DyLight 550 fluorophore (GxTX-550; Tilley et al., 2014). DyLight 550 has poor two-photon excitation properties, and for this study, it was replaced with Alexa Fluor

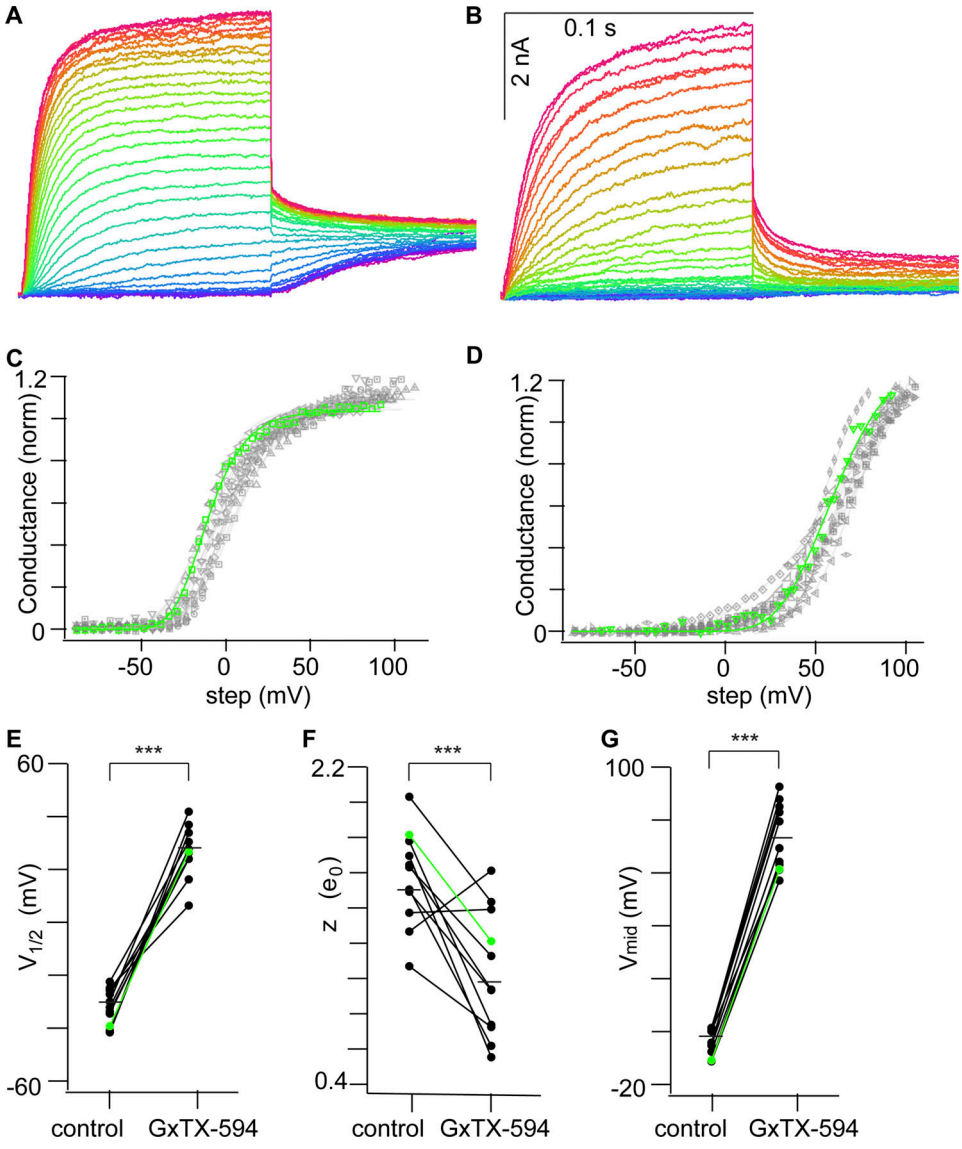

Figure 1. **GxTX-594 modulates Kv2.1 conductance. (A)** Representative Kv2.1-CHO current response under whole-cell voltage clamp. Cells were given 100-ms, 5-mV increment voltage steps ranging from −80 mV (blue) to +120 mV (red) and then stepped to 0 mV to record tail currents. The holding potential was −100 mV. **(B)** Kv2.1 currents from the same cell 5 min after the addition of 100 nM GxTX-594. Scale bars are the same for A and B. **(C)** Normalized conductance–voltage relationships from Kv2.1 tail currents before application of GxTX-594 (n = 13). Different symbols correspond to individual cells, and the green corresponds to cell in A. **(D)** Normalized conductance—voltage relationships in 100 nM GxTX-594 (n = 11). **(E)** Mean midpoint of each of four independent voltage sensors in the fourth-power Boltzmann fit ($V_{1/2}$) before (−31 ± 6 mV SD) and after (+27 ± 10 mV SD) 100 nM GxTX-594. ***, P < 0.0001 by Mann–Whitney U test. **(F)** Mean e_0 associated with Boltzmann fit (z) before (1.5 ± 0.3 e_0 SD) and after (1.0 ± 0.4 e_0 SD) 100 nM GxTX-594. ***, P = 0.0007 by Mann–Whitney U test. **(G)** Mean midpoint of conductance change in the fourth-power Boltzmann fit (V_{mid}) before (−2 ± 6 mV SD) and after (+73 ± 13 mV SD) 100 nM GxTX-594. ***, P < 0.0001 by Mann–Whitney U test.

594, a persulfonated Texas Red analogue with a large two-photon excitation cross section and ample spectral separation from GFP, making it well suited for multiplexed, two-photon excitation imaging experiments (Zito et al., 2004). We refer to this EVAP variant as GxTX-594.

We performed electrophysiological analyses to determine whether GxTX-594 retains the ability to allosterically modulate Kv2.1 (Fig. 1). GxTX is a partial inverse agonist of Kv2.1, which lowers channel open probability by stabilizing voltage sensors in a resting conformation. Consequently, more positive intracellular voltage is required to activate voltage sensors and achieve the same open probability as without GxTX (Tilley et al., 2019). Previously, we estimated that a Kv2.1 voltage sensor with GxTX bound is 5,400-fold more stable in its resting conformation and requires more positive intracellular voltage to become activated (Tilley et al., 2019). To characterize the efficacy of GxTX-594 in allosterically modulating Kv2.1 gating, we voltage clamped Kv2.1-CHO cells and measured K^+ currents in GxTX-594. We analyzed the Kv2.1 conductance–voltage (GV) relation by fitting with a fourth power Boltzmann function. The voltage at which the conductance of the fitted function is 50% of maximum, V_{mid}, was +73 ± 13 mV for 100 nM GxTX-594 (Fig. 1 G). For comparison, the V_{mid} of 100 nM GxTX was +67 ± 6 mV (Tilley et al., 2019). This shift of the GV indicates that GxTX-594 retains an efficacy similar to GxTX.

Table 1. **Parameters used for calculations to generate Scheme 1: EVAP allosteric expansion**

Parameter	Value
$k_{on,resting}$	0.30 μM^{-1} s^{-1}
$k_{off,resting}$	0.0081 s^{-1}
$k_{on,activated}$	0.21 $\mu M^{-1}s^{-1}$
$k_{off,activated}$	0.39 s^{-1}
$V_{1/2,unlabeled}$	−32 mV
$V_{1/2,labeled}$	41 mV
z	1.5 e_0

GxTX-594 labels Kv2 proteins

To determine the concentration range where GxTX-594 effectively labels Kv2.1 protein, we performed a concentration–effect experiment. As the K_d of our previously presented EVAP, GxTX-550, was 30.0 ± 3.9 nM at a holding potential of −100 mV (Tilley et al., 2014), we presumed that 1,000 nM would be a sufficient upper bound for concentration–effect experiments with GxTX-594 (Fig. 2, A and B). Cell surface fluorescence intensity was analyzed immediately after washout of 1, 10, 100, and 1,000 nM GxTX-594 to eliminate fluorescence from toxin in solution. This fluorescence labeling concentration–effect relation was fit with a Langmuir binding isotherm, resulting in a K_d of 26.9 ± 8.3 nM (Fig. 2 C). Due to the incomplete equilibration of labeling at 1 and 10 nM, our measure is expected to overestimate the K_d. The near saturation of the fluorescence concentration–effect relation with 100 nM GxTX-594, and the rate of fluorescence equilibration (Fig. 2 D) suggested that incubation with 100 nM GxTX-594 for 5 min results in near-maximal labeling on the glass-adhered surface of Kv2.1-CHO cells.

We assessed whether GxTX-594 fluorescence on CHO-K1 cells is due to the presence of Kv2 proteins. CHO-K1 cells were transfected with either a rat Kv2.1-GFP or Kv2.2-GFP construct, each of which yielded delayed rectifier K^+ currents (Fig. S2 A). 2 d after transfection, Kv2.1-GFP or Kv2.2-GFP fluorescence displayed distinct subcellular regions of high density at the glass-adhered surface (Fig. 3 A), which we refer to as Kv2 clusters, a term used to refer to similar high-density regions in neurons and other mammalian cell lines (Kirmiz et al., 2018b). Correlation coefficients indicated a high degree of subcellular colocalization of both Kv2 proteins with GxTX-594 (Fig. 3 B), quantitating the observation that GxTX-594 is not evenly distributed throughout the membrane but is localized to Kv2 clusters. We did not detect a significant difference between the ratios of GxTX-594 to Kv2.1-GFP or Kv2.2-GFP fluorescence (Fig. 3 C; P = 0.74 by Mann–Whitney *U* test), consistent with the lack of discrimination of GxTX between Kv2.1 and Kv2.2 (Herrington et al., 2006). GxTX accesses the membrane-embedded voltage sensors of Kv2 proteins by partitioning into the outer leaflet of the plasma membrane bilayer (Milescu et al., 2009; Gupta et al., 2015), and a GxTX derivative labeled with a fluorophore that brightens in less polar environments is detectable in the membrane of CHO cells without Kv2 proteins (Fletcher-Taylor et al., 2020). However, we failed to find any GxTX-594 labeling of CHO cells in the absence of Kv2 proteins (Fig. S3).

GxTX-594 selectively labels Kv2 proteins

An important consideration for determination of whether GxTX-594 could reveal conformational changes of endogenous Kv2 proteins is whether the EVAP is selective for Kv2 proteins. Electrophysiological studies have concluded that the native GxTX peptide is selective for Kv2 channels, with some off-target

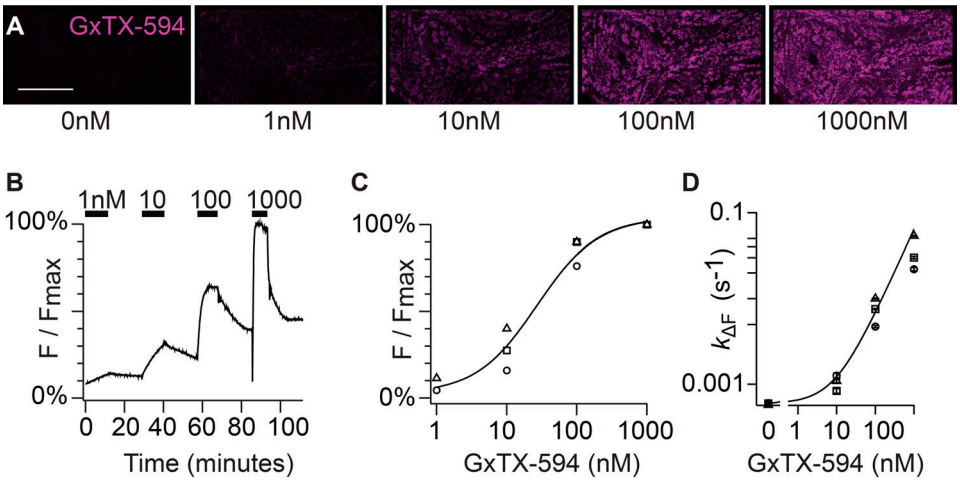

Figure 2. **Concentration–effect characteristics of GxTX-594 labeling. (A)** Fluorescence from confluent Kv2.1-CHO cells incubated in indicated concentrations of GxTX-594 for 15 min then washed out before imaging. Imaging plane was near the glass-adhered cell surface. Fluorescence shown corresponds to GxTX-594 (magenta). Scale bar, 20 µm. **(B)** Time-lapse fluorescence intensity from the concentration–effect experiment shown in A. Fluorescence was not background subtracted. F_{max} is intensity while cells were incubated in 1,000 nM GxTX-594. **(C)** Relative fluorescence intensity of GxTX-594 that remains on cells immediately after washout of indicated concentrations of GxTX-594 from the extracellular solution. Symbols correspond to each of three experiments. Black line is the fit of a Langmuir isotherm for K_d = 26.9 nM ± 8.3. **(D)** Labeling or unlabeling kinetics for GxTX-594 at indicated concentrations. Symbols correspond to the same experiments as panel C. $k_{\Delta F}$ values obtained from monoexponential fits (Eq. 1). Error bars represent the SD of $k_{\Delta F}$ fitting. Black line is fit of the $k_{\Delta F}$–concentration relation with Eq. 4, k_{on} = 6.372 × 10^{-5} ± 0.049 × 10^{-5} nM^{-1} s^{-1}; k_{off} = 5.929 × 10^{-4} ± 0.043 × 10^{-4} s^{-1}.

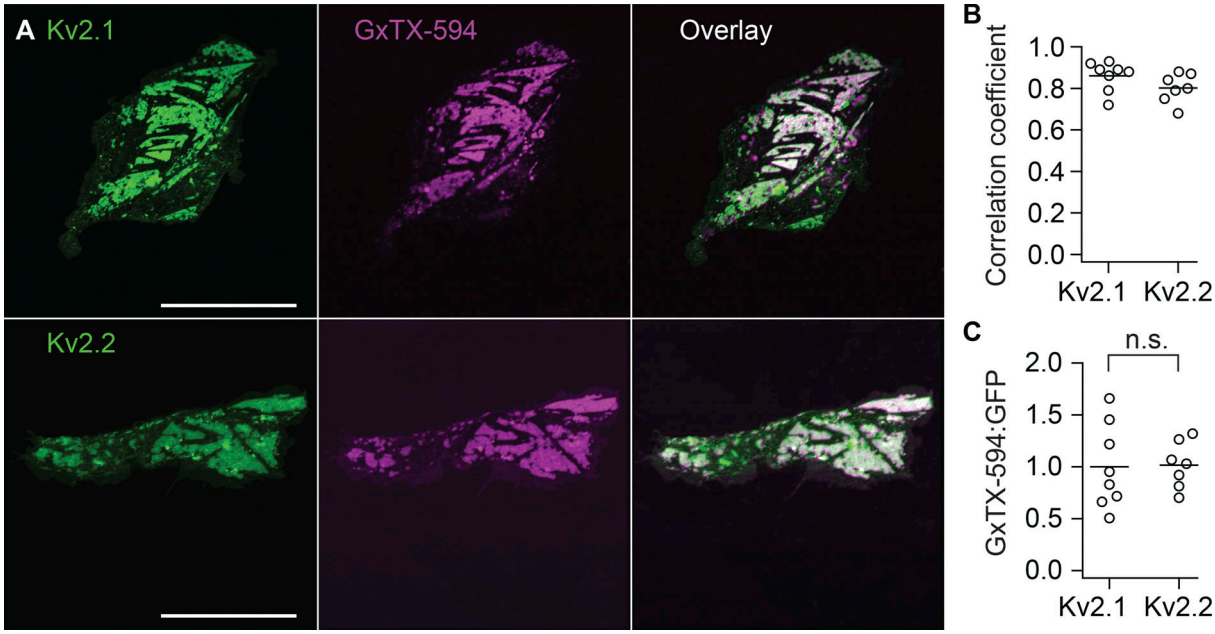

Figure 3. **GxTX-594 colocalizes with Kv2-GFP. (A)** Fluorescence from CHO cells transfected with Kv2.1-GFP (top) or Kv2.2-GFP (bottom) and labeled with GxTX-594. Optical sections were near the glass-adhered cell surface. Cells were incubated with 100 nM GxTX-594 for 5 min and rinsed before imaging. Fluorescence shown corresponds to emission of GFP (left), GxTX-594 (middle), or as an overlay of GFP and GxTX-594 (right). Scale bars, 20 µm. **(B)** Pearson correlation coefficients for GxTX-594 colocalization with Kv2.1-GFP or Kv2.2-GFP. **(C)** Ratio of fluorescence intensity of the same cells in B when excited at 594 nm versus 488 nm from cells expressing Kv2.1-GFP or Kv2.2-GFP. In B and C, pixel intensities were background subtracted before analyses by subtracting the average fluorescence of a background ROI that did not contain cells from the ROI containing the cell. Circles represent measurements from individual cells, and each transfection group contains data from two separate applications of GxTX-594. Bars represent the mean. No significant difference was detected between Kv2.1-GFP or Kv2.2-GFP by Mann–Whitney *U* test (P = 0.74).

modulation of A-type Kv4 channels (Herrington et al., 2006; Liu and Bean, 2014; Speca et al., 2014). However, electrophysiological testing cannot determine whether ligands bind unless they also alter currents (Sack et al., 2013). Furthermore, structural differences between wild-type GxTX and the GxTX-594 variant could potentially alter selectivity among channel protein subtypes.

To test whether GxTX-594 binds other voltage-gated K^+ channel subtypes, we quantified surface labeling and analyzed colocalization of GxTX-594 with a selection of GFP-tagged voltage-gated K^+ channel subtypes (Fig. 4 A). The ratio of GxTX-594 fluorescence to each GFP-tagged K^+ channel subtype was not distinguishable from zero for Kv4.2, Kv1.5, or BK channels (Fig. 4 B), indicating minimal, if any, binding. Furthermore, no colocalization was apparent between Kv4.2, Kv1.5, or BK channels and the residual GxTX-594 fluorescence (Fig. 4 C). An additional set of experiments conducted under different microscopy conditions and without the auxiliary subunits of Kv4.2 or Kv1.5 also gave no indication of GxTX-594 labeling (Fig. S2). While we cannot be certain that GxTX-594 does not bind any of the >80 known mammalian proteins containing voltage sensor domains, the lack of labeling of the related voltage-gated K^+ channels indicates that GxTX-594 does not promiscuously label voltage sensors.

The relationship between GxTX-594 cell-surface fluorescence and Kv2.1 voltage activation

To understand the relationship between channel gating and GxTX-594 fluorescence, we determined how fluorescence intensity on cells expressing Kv2.1 responds to changes in membrane voltage. We found that GxTX-594 equilibrated more quickly on the sides of cells than on their glass-adhered surface, presumably due to restricted access to the extracellular space by the glass (Fig. S4). Due to this observation, we chose an imaging plane where fluorescence from GxTX-594 resembled an annulus (Fig. 6 A). This imaging plane varied between cells but was >1 µm above the glass. We developed a labeling protocol in which Kv2.1-CHO cells were incubated for 5 min in a bath solution (CEG) containing 100 nM GxTX-594, which was then diluted with extracellular solution to 9 nM (Fig. 5). Once GxTX-594 fluorescence intensity stabilized at the cell membrane (at least 9 min; Fig. 5), cells were voltage clamped in whole-cell mode. We measured the fluorescence response of GxTX-594 when the membrane voltage of Kv2.1-CHO cells was stepped from a holding potential of −80 mV to more positive voltages that ranged from −40 mV to +80 mV (Fig. 6 A). ROIs corresponding to the cell surface were manually identified and average fluorescence intensity quantified from time-lapse sequences. The voltage-dependent reduction in fluorescence equilibrates to a value above background. Even when cells were given a +80-mV depolarizing voltage stimulus, some GxTX-594 fluorescence remained (Fig. 6 B). Most of the residual fluorescence appeared to be localized to the cell surface membrane (Fig. 6 A) and varied between cells (Fig. 6 C). As such surface labeling was not present on CHO cells in the absence of Kv2 proteins (Fig. S3), we consider this residual fluorescence to originate from voltage-insensitive Kv2 proteins. Voltage-insensitive fluorescence

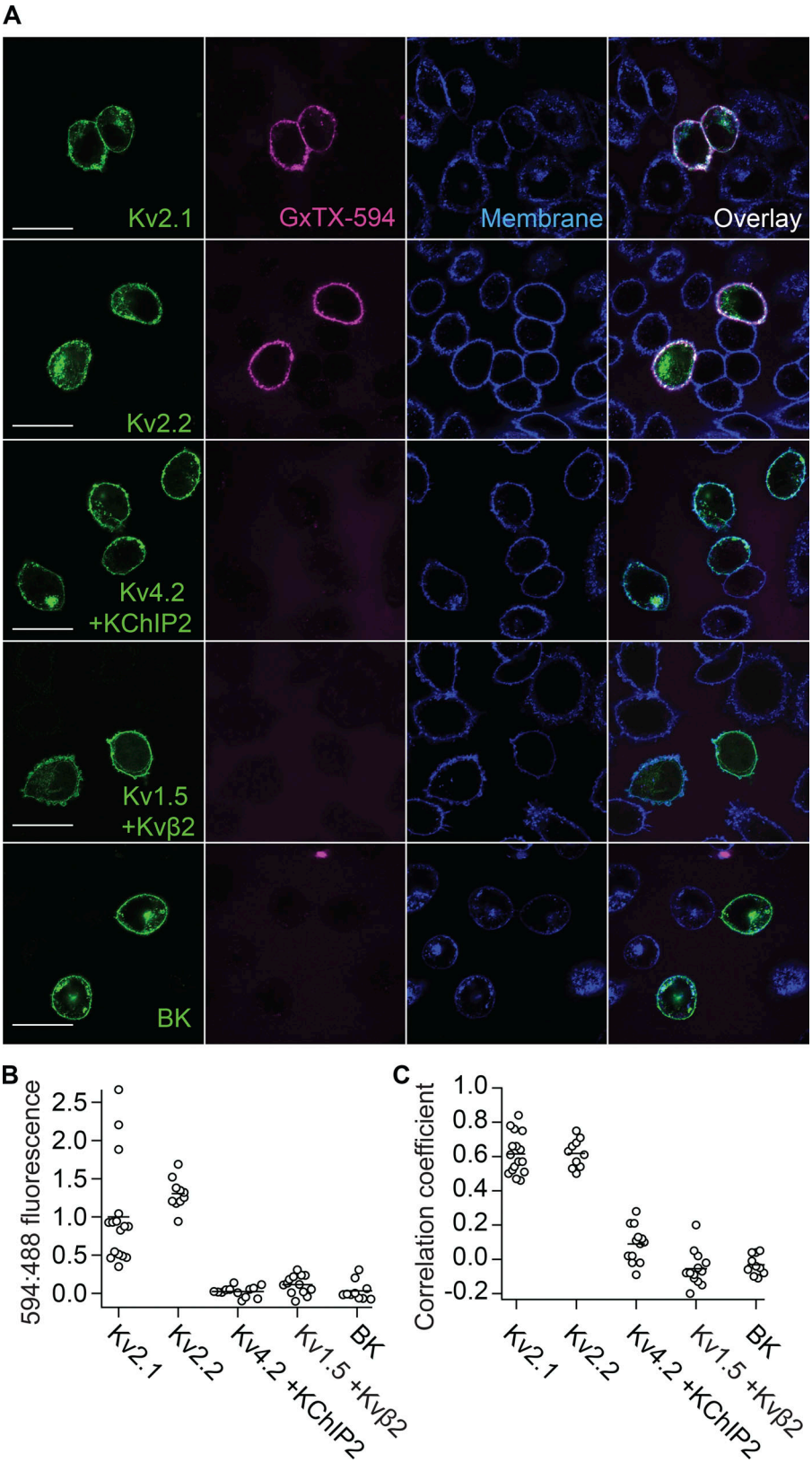

Figure 4. **GxTX-594 selectively labels Kv2 proteins. (A)** Fluorescence from live CHO cells transfected with Kv2.1-GFP, Kv2.2-GFP, Kv4.2-GFP + KChIP2, Kv1.5-GFP + Kvβ2, or BK-GFP (indicated by row) and labeled with GxTX-594. Airy disk imaging was from a plane above the glass-adhered surface. Cells were incubated with 100 nM GxTX-594 and 5 µg/ml WGA-405 then rinsed before imaging. Fluorescence corresponds to emission of GFP (column 1), GxTX-594 (column 2), WGA-405 (column 3), or an overlay (column 4). Scale bars, 20 µm. **(B)** Intensity of GxTX-594 labeling for different K^+ channel-GFP types. Fluorescence intensity resulting from 594-nm excitation of GxTX-594 is divided by fluorescence intensity resulting from 488-nm excitation of GFP. This value was normalized to the average 594:488 ratio from GxTX-594 and Kv2.1-GFP. Circles indicate measurements from individual cells. Only cells with obvious GFP expression were analyzed. For analysis, ROIs were drawn around the cell membrane indicated by WGA-405 fluorescence. Pixel intensities were background subtracted before analyses by subtracting the average fluorescence of a background ROI that did not contain cells from the ROI containing the cell; this occasionally resulted in ROIs with negative intensity. Kv2.1, n = 16; Kv2.2, n = 10; Kv4.2, n = 13; Kv1.5, n = 13; and BK, n = 10; n indicates the number of individual cells analyzed in a single dish during a single application of GxTX-594 with the indicated K^+ channel-GFP type. Bars represent the mean. Significant differences were observed between 594:488 ratio for Kv2.1 or Kv2.2 and Kv1.5, Kv4.2, or BK by Mann–Whitney U test ($P < 0.0001$). The P value to determine significance is adjusted for multiple comparisons using the Bonferroni method, where $P < 0.0033$ is considered significant, with the caveat that data points under each condition are technical replicates. **(C)** Pearson correlation coefficients between GxTX-594 and GFP. Same cells as B. Significant differences were observed between correlation coefficients for Kv2.1 or Kv2.2 and Kv1.5, Kv4.2, or BK by Mann-Whitney U test ($P < 0.0001$).

could potentially be from Kv2.1–GxTX-594 complexes with immobilized voltage sensors or internalized Kv2.1–GxTX-594 complexes that remain just under the cell surface (Deutsch et al., 2012; Weigel et al., 2012; Fox et al., 2013a; Weigel et al., 2013).

To compare voltage response properties between cells, we used a normalization procedure to analyze only the voltage-sensitive fraction of the fluorescence from each cell, which we defined as the fluorescence that changed between −80 mV and

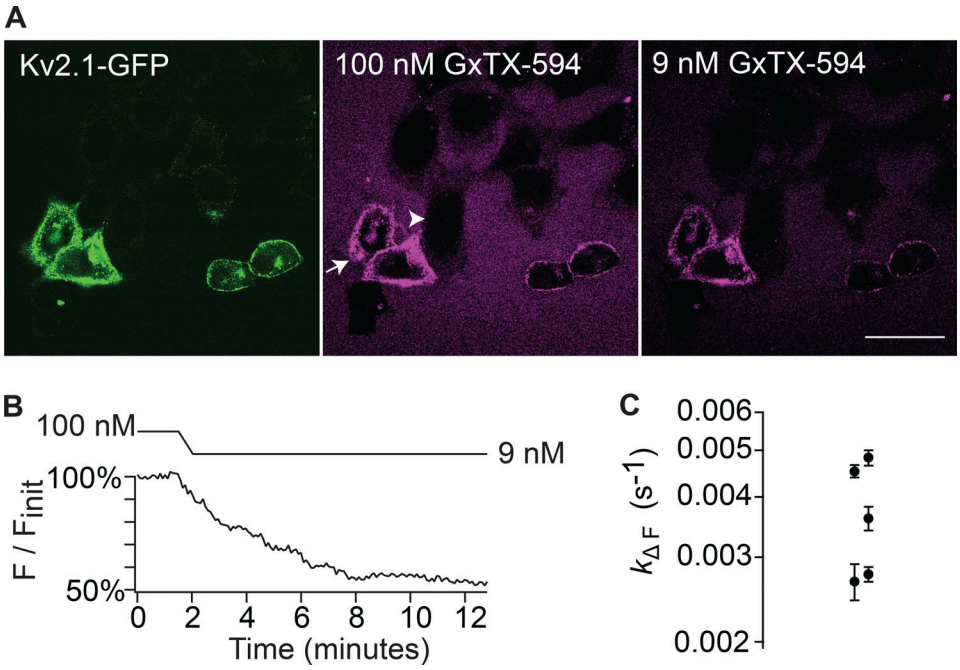

Figure 5. **GxTX-594 fluorescence equilibration after dilution from 100 nM to 9 nM. (A)** CHO cells transfected with Kv2.1-GFP (left) in 100 nM GxTX-594 (middle) and after dilution to 9 nM GxTX-594 (right). Regions darker than the background bath solution are CHO cells not transfected with Kv2.1-GFP (arrowhead). Scale bar, 20 µm. **(B)** Fluorescence excited at 594 nm during dilution from 100 nM GxTX-594 to 9 nM GxTX-594. Timing of dilution is shown above the graph. Fluorescence was normalized to the mean 594 fluorescence before dilution to 9 nM. Data are from the cell labeled with an arrow in A. 100 nM and 9 nM images in A are from 0 and 12 min, respectively. **(C)** Rate of GxTX-594 fluorescence decay after dilution. Error bars are SDs of $k_{\Delta F}$ fit. n = 5 cells.

+80 mV. The initial fluorescence at a holding potential of −80 mV was normalized to 100% F/F_{init}, and residual fluorescence after a +80-mV step was normalized to 0% F/F_{init} (Fig. 6 D). To characterize the voltage dependence of the Kv2.1–GxTX-594 interaction, fluorescence–voltage (FV) responses were fit with a Boltzmann distribution (Eq. 2). This fit had a half maximal voltage midpoint ($V_{1/2}$) of −27 mV and a steepness (z) of 1.4 e_0 (Fig. 6 D, bottom panel, black line). This is similar to voltage sensor movement in Kv2.1-CHO cells without any GxTX present: $V_{1/2}$ = −26 mV, z = 1.6 e_0 (Tilley et al., 2019). These results suggest that at 9 nM GxTX-594, the FV appears to be a good surrogate for the gating current–voltage (QV) response of unlabeled Kv2 channels.

To determine the voltage dependence of the kinetics of GxTX-594 labeling and unlabeling, we compared $k_{\Delta F}$ at varying step potentials. We quantified $k_{\Delta F}$ by fitting the average fluorescence from voltage-clamped cells with a monoexponential function (Eq. 1). In response to voltage steps from a holding potential of −80 mV to more positive potentials, $k_{\Delta F}$ increased progressively as step potential was increased above −40 mV and appeared to begin to saturate at higher voltages (Fig. 6 E). Upon return to −80 mV, $k_{\Delta F}$ was similar to −40 mV. While the $k_{\Delta F}$ did not clearly display saturation at positive voltages that would justify fitting with a Boltzmann function, a model of GxTX-594 dynamics, which we develop later in this study, indicated that Boltzmann fitting could yield physical insight (Fig. 6 E, bottom panel, black line). We noted that the degree of variability in $k_{\Delta F}$ measurements became greater at more positive potentials (Fig. 6 E, top and bottom panels). At −80 mV, there was a twofold range in $k_{\Delta F}$ values and a ninefold range at +80 mV. The relatively low variation in $k_{\Delta F}$ at −80 mV suggests that despite variance in fluorescence intensity after rebinding (Fig. S4 C), $k_{\Delta F}$ from fits of the upward relaxation at −80 mV are relatively consistent. The average $k_{\Delta F}$ equilibration at 10 nM GxTX-594 in concentration–effect experiments was comparable to Kv2.1-CHO cells incubated in 9 nM GxTX-594 and voltage clamped at −80 mV (0.0011 s^{-1} and 0.0014 s^{-1}, respectively; Fig. S4 E and Fig. 2 D). This suggests that the Kv2 voltage sensors in the unclamped cells for concentration–effect experiments are in the same early resting conformation as voltage-clamped cells at −80 mV. Additionally, we determined that only a small fraction of the up to ninefold variability in $k_{\Delta F}$ at positive voltages could be attributed to temperature fluctuations (Fig. S5). Possible reasons for cell-to-cell variability at more positive voltages are discussed further in Limitations.

The relation between voltage sensor activation and GxTX-594 dynamics can be recapitulated by rate theory modeling

To enable translation of the intensity of fluorescence from GxTX-594 on a cell surface into a measure of Kv2 conformational change, we developed an EVAP model, a series of equations derived from rate theory that relate cell labeling to voltage sensor activation. The framework of the EVAP model is generalizable to fluorescent molecular probes that report conformational changes by a change in binding affinity. In the EVAP model, the proportion of labeled versus unlabeled Kv2 in a membrane is determined by the proportion of voltage sensors in resting versus activated conformations. The model assumes that the innate voltage sensitivity of the Kv2 subunit is solely

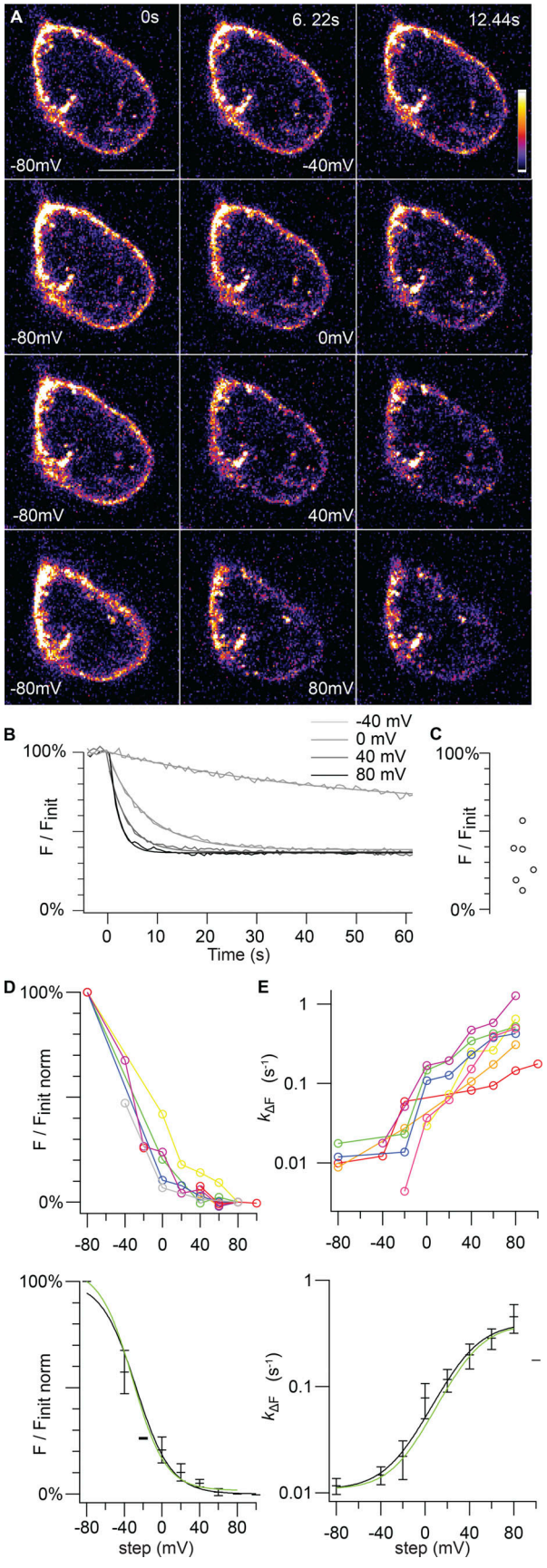

Figure 6. **GxTX-594 labeling responds to transmembrane voltage.** **(A)** Fluorescence from an optical section of a voltage-clamped Kv2.1-CHO cell in 9 nM GxTX-594. Color progression for pseudocoloring of fluorescence intensity is shown in vertical bar on right. Middle column in each row indicates voltage step taken from a holding potential of −80 mV. Times listed at top of each column correspond to time axis in panel B. Scale bar, 10 µm. **(B)** GxTX-594 fluorescence during steps to indicated voltages. Smooth lines are mono-exponential fits (Eq. 1): −40 mV $k_{\Delta F}$ = 2.15 × 10^{-2} ± 0.22 × 10^{-2} s^{-1}; 0 mV $k_{\Delta F}$ = 1.279 × 10^{-1} ± 0.023 × 10^{-1} s^{-1}; 40 mV $k_{\Delta F}$ = 2.492 × 10^{-1} ± 0.062 × 10^{-1} s^{-1}; and 80 mV $k_{\Delta F}$ = 4.20 × 10^{-1} ± 0.11 × 10^{-1} s^{-1}. ROIs were hand-drawn around the apparent cell surface membrane based on GxTX-594 fluorescence. 0% was set by subtraction of background, which was the average intensity of a region that did not contain cells over the time course of the voltage protocol. For each trace, 100% was set from the initial fluorescence intensity at −80 mV before the subsequent voltage step. Raw initial fluorescence values before normalization were within 10% of one another. **(C)** Fluorescence intensity remaining at the end of 50-s steps to +80 mV. Each circle represents one cell. Background subtraction as in B. **(D)** Voltage dependence of fluorescence intensity at the end of 50-s steps. For each cell, 100% was set from the initial fluorescence intensity at −80 mV before the first step to another voltage. Cells did not always recover to initial fluorescence intensity during the −80-mV holding period between voltage steps. Top: Circle coloring indicates data from the same cell, and lines connect points from the same cell. Gray circles represent data shown in B. Bottom: Black bars represent the mean F/F_{init} at each voltage, and error bars represent the SEM. Black line is the fit of a first-order Boltzmann equation (Eq. 2): $V_{1/2}$ = −27.4 ± 2.5 mV, z = 1.38 ± 0.13 e_0. Green line is the prediction from the EVAP model at 9 nM GxTX. **(E)** Voltage dependence of fluorescence intensity kinetics ($k_{\Delta F}$). Top: Circle coloring is the same as D. Bottom: Black bars represent the average $k_{\Delta F}$ at each voltage, and error bars represent the SEM. Black line is a first-order Boltzmann equation fit to the $k_{\Delta F}$–voltage relation: $V_{1/2}$ = +38 ± 15 mV, z = 1.43 ± 0.35 e_0. Green line is the prediction from the EVAP model at 9 nM GxTX.

responsible for controlling voltage dependence. EVAP labeling is voltage dependent because the binding and unbinding rates are different for resting and activated conformations of voltage sensors. Voltage activation of Kv2 channels involves many conformational changes (Scholle et al., 2004; Jara-Oseguera et al., 2011; Tilley et al., 2019). However, models that presume independent activation of a voltage sensor in each of the four Kv2.1 subunits accurately predict many aspects of voltage activation and voltage sensor toxin binding (Lee et al., 2003; Tilley et al., 2019). For simplicity, we model Kv2 proteins as having only resting and activated conformations that are independent in each voltage sensor and developed a rate theory model consisting of four interconnected states (Scheme 1).

When voltage sensors change from resting to activated conformations, the binding rate of the GxTX-594 EVAP decreases, and the unbinding rate increases. When the membrane voltage is held constant for sufficient time, the proportions of labeled and unlabeled proteins reach an equilibrium. EVAP labeling requires seconds to equilibrate (Fig. 6), whereas Kv2 channel gating equilibrates in milliseconds (Tilley et al., 2019), three orders of magnitude more quickly. These distinct time scales of equilibration suggest an approximation to model the reversible EVAP labeling response: voltage sensor conformations achieve equilibrium quickly such that only their distribution at equilibrium is expected to greatly impact the kinetics of labeling and unlabeling, allowing Scheme 1 to collapse into Scheme 2, which depicts the structure of the EVAP model used for calculations.

We constrained the EVAP model with measurements of GxTX-594 binding kinetics and GxTX impacts on Kv2.1 gating

(see EVAP model and Data S1). We tested the viability of model predictions by comparison with GxTX-594 labeling measurements. The EVAP model predicts that the *FV* for GxTX-594 labeling will conform to a Boltzmann distribution. The *FV* prediction in 9 nM GxTX-594 had a $V_{1/2}$ and z that differ by only −4 mV and 0.06 e_0, respectively, from the Boltzmann fit of experimental data (Fig. 6 D, bottom panel, black and green lines). The EVAP model also predicts that the $k_{\Delta F}$-V will conform to a Boltzmann distribution. The $k_{\Delta F}$-V prediction differs by only 3 mV and 0.05 e_0 from the Boltzmann fit of experimental data (Fig. 6 E, bottom panel, blue line). However, this fit was poorly constrained as we failed to obtain sufficient data at voltages above +80 mV where $k_{\Delta F}$-V is predicted to saturate. In our attempts, the durations required at more positive voltages irreversibly increased membrane leak. The $V_{1/2}$ and z values from the GxTX-594 *FV* and $k_{\Delta F}$-V were not used as constraints of the EVAP model, and the similarity between the predictions and empirical findings seemed remarkable enough to warrant further exploration of the EVAP model predictions.

We used the EVAP model to investigate general principles of the relation between voltage sensor activation and reversible labeling. The EVAP model predicts that as GxTX-594 concentration decreases, the change in labeling ($\Delta F/\Delta F_{max}$) approaches the probability that unlabeled voltage sensors are resting (Fig. 7 A). This prediction explains the similarity between the *FV* in 9 nM GxTX-594 ($V_{1/2}$ = −27 ± 3 mV, z = 1.4 ± 0.1 e_0; Fig. 6 D) and the *QV* of Kv2.1 ($V_{1/2}$ = −26 ± 1 mV, z = 1.6 ± 0.1 e_0; Tilley et al., 2019). As the concentration of EVAP is increased, the *FV* shifts to more positive voltages such that the fractional change in fluorescence intensity is always less than the fraction of unlabeled voltage sensors that are active. As EVAP concentration increases and approaches the activated state K_d (1,790 nM), voltage sensor activation becomes less effective at dissociating the EVAP due to binding to activated voltage sensors (Fig. 7 B). The model predicts that at any concentration, this simple interpretation will be valid: A decrease in EVAP surface fluorescence indicates activation of unlabeled voltage sensors.

The EVAP model also yields a simple interpretation of labeling kinetics, it predicts that as GxTX-594 concentration decreases, the rate of fluorescence change $k_{\Delta F}$ approaches the probability that labeled channels are active (Fig. 7 C). This prediction explains the similarity between the $k_{\Delta F}$-V in 9 nM GxTX-594 ($V_{1/2}$ = 38 ± 15 mV, z = 1.4 ± 0.4 e_0; Fig. 6 D) and the *QV* of Kv2.1 in saturating GxTX ($V_{1/2}$ = 47 ± 1 mV, z = 1.6 ± 0.1 e_0; Tilley et al., 2019). At low concentrations, the dependence of $k_{\Delta F}$ on the conformation of channels bound to GxTX-594 is due to the rate of unbinding dominating $k_{\Delta F}$, with the rate of unbinding being solely determined by the conformation of channels bound to GxTX-594.

Repetitive action potential–like stimuli amplify the GxTX-594 response

Kv2 currents impact repetitive action potential firing (Du et al., 2000; Liu and Bean, 2014), making repetitive action potentials the voltage waveforms that are, arguably, most relevant to Kv2 function. However, action potentials occur on the millisecond time scale, orders of magnitude faster than the GxTX-594 response, which integrates Kv2 conformations occurring over many seconds. Kv2 channels have slow deactivation kinetics (Liu and Bean, 2014; Tilley et al., 2019), and high-frequency firing could prevent Kv2 proteins from fully deactivating before a next action potential is triggered, creating a kinetic trap that progressively accumulates activated voltage sensors. This behavior of Kv2 proteins indicates that high-frequency firing could evoke a more robust fluorescence signal than the EVAP model predicts, as the model assumes continuous equilibrium of voltage sensors and cannot kinetically trap activated conformations. To test this hypothesis, we crudely mimicked action potentials with trains of 2-ms voltage steps from −80 to +40 mV and observed the changes in fluorescence on GxTX-594–labeled Kv2.1-CHO cells (Fig. 8, A and B). To assess frequency response, step frequency was varied from 0.02 to 200 Hz. GxTX-594 unlabeling and $k_{\Delta F}$ increased with stimulus frequency (Fig. 8, C and D). We compared these fluorescence responses to those predicted by the EVAP model.

When the stimulus frequency was <50 Hz, the EVAP model did a reasonable job of predicting fluorescence change. At and >50 Hz, fluorescence decreased by more than the EVAP model predicted, even without accounting for a voltage-insensitive fraction of Kv2.1 proteins (Fig. 8 C, bottom panel, green line). As discussed above, this divergence from the equilibrium-based EVAP model is expected at frequencies where voltage steps are shorter than Kv2 equilibration times. The time constant of activating gating current decay from Kv2.1-CHO cells was 1.3 ms at +40 mV (Tilley et al., 2019), which means that the majority of voltage sensors are effectively activated during the 2-ms +40 mV steps. In contrast, the time constant of deactivating gating current decay from Kv2.1-CHO cells was 22 ms at −80 mV (Tilley et al., 2019), which means that Kv2.1 is expected to become kinetically trapped in activated conformations when stimuli to +40 mV from −80 mV are ∼50 Hz or faster. Thus, the amplified EVAP response appears consistent with voltage sensors failing to deactivate before the next stimulus, leading to an accumulation of activated voltage sensors and a more dramatic fluorescence response than predicted by the EVAP model. Overall, these dynamics indicate that the magnitude of the change in GxTX-594 fluorescence intensity will be amplified during repetitive action potentials, a regimen of electrophysiological signaling where Kv2 currents are critical.

In contrast, the kinetics of the GxTX-594 response did not appear to deviate from EVAP model predictions at high frequencies (Fig. 8 D). As $k_{\Delta F}$ responds to the dynamics of Kv2 proteins bound by GxTX-594, it could be that the faster deactivation rate of voltage sensors bound by GxTX (Tilley et al., 2019) prevents the bound channels from being kinetically trapped.

GxTX-594 labels brain slices transfected with Kv2.1-GFP

To determine whether expression of Kv2 proteins embedded in tissue can be imaged with GxTX-594, we overexpressed Kv2.1-GFP in rat brain slices and examined CA1 pyramidal neurons of the hippocampus. We chose CA1 neurons for several reasons: They express Kv2 channels at a density typical of central neurons, the physiology of these neurons has been intensively studied, and their electrical properties are relatively homogeneous

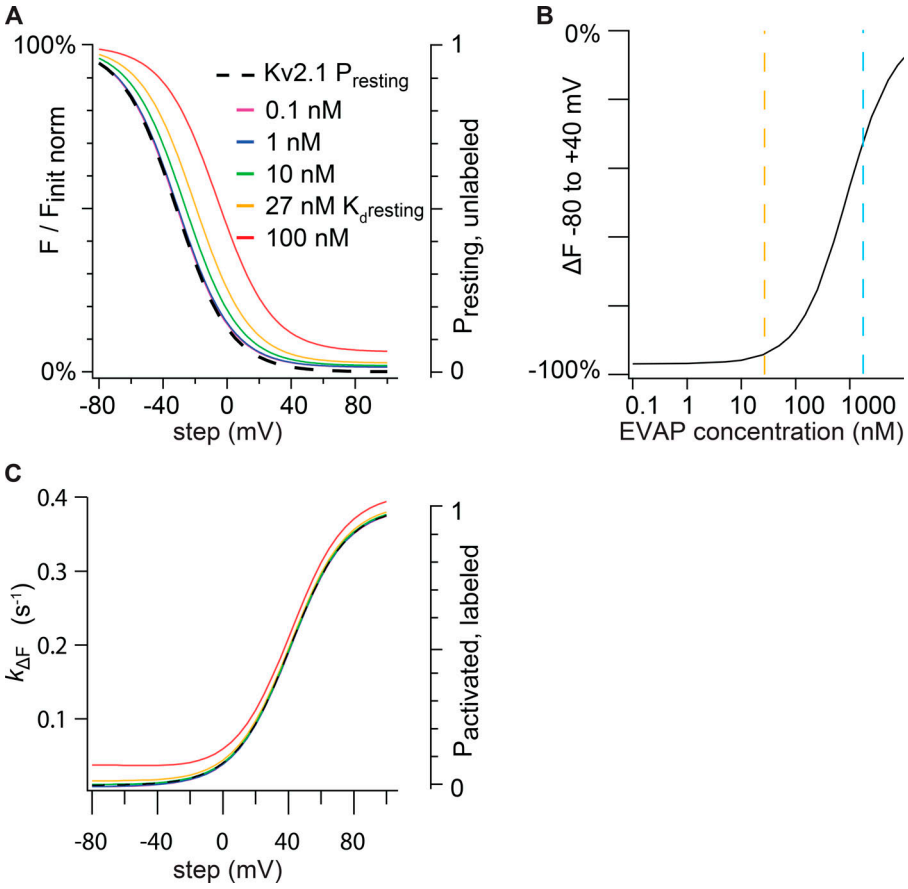

Figure 7. **Relationship of GxTX-594 labeling to probability of Kv2 voltage sensor activation. (A)** EVAP model predictions of concentration and voltage dependence of cell surface fluorescence intensity at different concentrations of EVAP in solution. The bottom axis represents membrane voltage. The left axis represents the predicted fluorescence relative to when all voltage sensors are at rest (F_{init}) and does not include EVAP signal that is insensitive to voltage. The dashed line corresponds to the right axis and represents the probability that voltage sensors of unlabeled Kv2.1 are in their resting conformation. **(B)** EVAP model prediction of the cell surface fluorescence when cells are given a +40-mV depolarization relative to when all voltage sensors are at rest (F_{init}) at increasing concentrations of EVAP. The orange dashed line represents K_d of resting voltage sensors. The blue dashed line represents K_d of activated voltage sensors. **(C)** EVAP model predictions of concentration and voltage dependence of $k_{\Delta F}$. Colors correspond to A, except the dashed line is the probability that voltage sensors bound by GxTX-594 are an activated conformation.

(Misonou et al., 2005). Organotypic hippocampal slice cultures prepared from postnatal day 5–7 rats were sparsely transfected with Kv2.1-GFP, resulting in a subset of neurons displaying green fluorescence. When imaged 2–4 d after transfection, GFP fluorescence was observed in the plasma membrane surrounding neuronal cell bodies and proximal dendrites (Fig. S6, A and B). Six days or more after transfection, Kv2.1-GFP fluorescence organized into clusters on the surface of the cell soma and proximal processes (Fig. 9 A and Fig. S6 C), a pattern consistent with a prior report of endogenous Kv2.1 in CA1 neurons (Misonou et al., 2005). After identifying a neuron expressing Kv2.1-GFP, solution flow into the imaging chamber was stopped, and GxTX-594 was added to the static bath solution to a final concentration of 100 nM. After 5 min of incubation, solution flow was restarted, leading to washout of excess GxTX-594 from the imaging chamber. After washout, GxTX-594 fluorescence remained colocalized with Kv2.1-GFP (Fig. 9 and Fig. S6), indicating that GxTX-594 is able to permeate through dense neural tissue and bind to Kv2 proteins on neuronal surfaces. Pearson correlation coefficients confirmed the colocalization of GxTX-594 with Kv2.1-GFP in multiple slices (Fig. 9 C). In most images of Kv2.1-GFP–expressing neurons, GxTX-594 also labeled puncta on neighboring neurons that did not express Kv2.1-GFP but at intensities that were roughly an order of magnitude dimmer (Fig. 9 B, white arrow). The clustered GxTX-594 fluorescence patterns on the cell body and proximal processes of CA1 neurons were strikingly similar to reported patterns of anti-Kv2 immunofluorescence patterns and are consistent with GxTX-594 labeling of endogenous Kv2 proteins in CA1 neurons. While we cannot exclude the possibility that CA1 neurons have a subset of Kv2 proteins on their surface that is not labeled by GxTX-594, we saw no indication of Kv2.1-GFP on neuronal surfaces that are not labeled by GxTX-594.

While we observed GxTX-594 fluorescence that morphologically resembles endogenous Kv2 protein localizations, we also found that GxTX-594 occasionally labels structures not consistent with Kv2 proteins (Fig. S6, bottom panel, arrows). This non-Kv2 labeling was most prevalent at the surface of the hippocampal slices and progressively decreased as the imaging plane was moved deeper into the tissue (data not shown). Our interpretation of this phenomenon is that GxTX-594 can accumulate in the dead tissue and debris that is present at the surface of a hippocampal section after it is cut. For this reason, we analyzed only GxTX-594 fluorescence with subcellular localizations consistent with Kv2 channels.

GxTX-594 labeling in brain slices responds to neuronal depolarization

To test whether reversible GxTX-594 labeling of neurons in brain slices is consistent with binding to endogenous Kv2 voltage sensors, we determined whether GxTX-594 labeling responds to voltage changes in tissue. First, we looked for Kv2-like patterns on CA1 pyramidal neurons in untransfected brain slices bathed in 100 nM GxTX-594. With two-photon excitation,

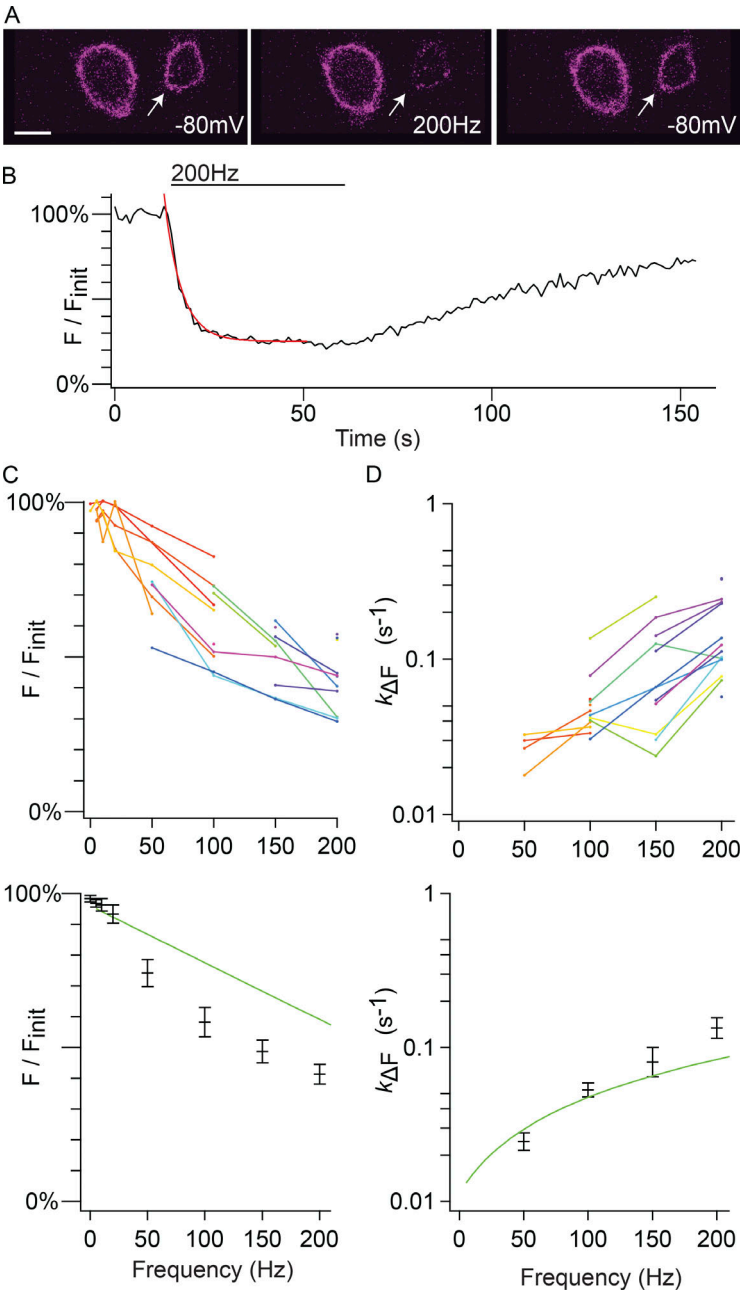

Figure 8. **High-frequency repetitive stimuli amplify the GxTX-594 response. (A)** Fluorescence intensity from Kv2.1-CHO cells incubated in 9 nM GxTX-594. Arrow indicates voltage-clamped cell. Fluorescence at holding potential of −80 mV (left), after 50 s of 200-Hz stimulus (middle), and 100 s after the cell is returned to holding potential of −80 mV (right). Stimulus was a 2-ms step to +40 mV. Note that in each panel, the unclamped cell (left cell in each panel) does not show a change in fluorescence. Scale bar, 10 µm. **(B)** Representative trace with GxTX-594 unlabeling at 200 Hz. Red line, monoexponential fit (Eq. 1): $k_{\Delta F}$ = 0.2327 ± 0.0099 × 10^{-1} s^{-1}. 0% F/F_{init} was set by subtraction of the average intensity of a region that did not contain cells. 100% was set by the initial fluorescence intensity at −80 mV. **(C)** Fluorescence–stimulus frequency relation. Points indicate F/F_{init} from individual cells. Top: Point coloring indicates data from the same cell. Bottom: Black bars represent the average F/F_{init} at each voltage, and error bars represent the SEM. Green line is the prediction of the EVAP model at a concentration of 9 nM. **(D)** $k_{\Delta F}$–stimulus frequency relation. Plotted as in C.

optical sections are thinner than the neuronal cell bodies, and GxTX-594 fluorescence appeared as puncta circumscribed by dark intracellular spaces (Fig. 10 A). This was similar to the patterns of fluorescence in Kv2.1-GFP–transfected slices (Fig. 9 B) and consistent with the punctate expression pattern of Kv2.1 in CA1 pyramidal neurons seen in fixed brain slices (Misonou et al., 2005).

We tested whether the punctate fluorescence was voltage sensitive using voltage clamp. To ensure voltage clamp of the neuronal cell body, slices were bathed in tetrodotoxin to block Na^+ channels, and Cs^+ was included in the patch pipette solution to block K^+ currents. In each experiment, whole-cell configuration was achieved with a GxTX-594–labeled neuron, and holding potential was set to −70 mV. At this point, time-lapse imaging of a two-photon excitation optical section was initiated. Depolarization to 0 mV resulted in loss of fluorescence from a subset of puncta at the perimeter of the voltage-clamped neuron (Fig. 10 B, red arrows; and Video 1). Other fluorescent puncta appeared unaltered by the 0-mV step (Fig. 10 B, white arrows). These puncta could represent Kv2 proteins on a neighboring cell, off-target labeling by GxTX-594, or voltage-insensitive Kv2 proteins, possibly due to near-surface internalization. To assess whether the fluorescence changes were due to the voltage change, we compared fluorescence of the apparent cell membrane region with regions more distal from the voltage-clamped cell body. An ROI 30-pixels (1.2-µm) wide containing the apparent membrane of the cell body was compared with other regions within each image (Fig. 10 C). The region containing the membrane of the cell body lost fluorescence during the 0-mV step (Fig. 10 D, ROI 1), while neither of the regions more distal

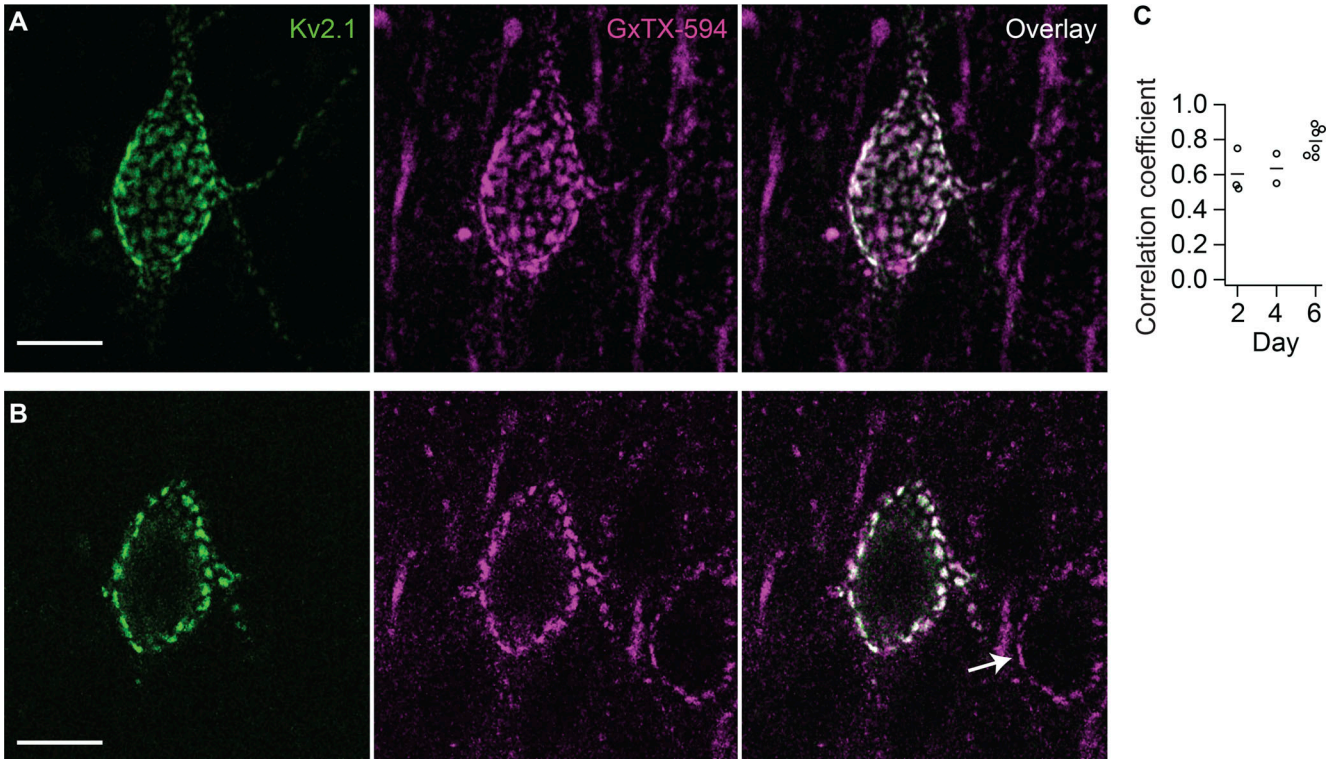

Figure 9. **GxTX-594 labels CA1 hippocampal pyramidal neurons transfected with Kv2.1-GFP. (A)** Two-photon excitation images of fluorescence from the soma and proximal dendrites of a rat CA1 hippocampal pyramidal neuron in a brain slice 6 d after transfection with Kv2.1-GFP (left), labeled with 100 nM GxTX-594 (middle), and the overlay (right). Image represents a Z-projection of 20 optical sections. Scale bar, 10 µm. **(B)** A single optical section of the two-photon excitation image shown in A. GxTX-594 labels both Kv2.1-GFP puncta from a transfected cell and apparent endogenous Kv2 proteins from an untransfected cell in the same cultured slice (right, arrow). Scale bar, 10 µm. **(C)** Pearson correlation coefficients from CA1 hippocampal neurons 2, 4, and 6 d after transfection with Kv2.1-GFP. Each circle represents a different neuron. Bars are arithmetic means.

(ROI 2, ROI 3) or the intracellular region (ROI 0) showed a similar change. In three hippocampal slices from separate rats, we found a significant decrease in fluorescence in ROI 1 compared with ROI 2 and ROI 3 when neurons were given a voltage step to 0 mV (Fig. 10 E; ANOVA $P < 0.001$; Tukey's post hoc test $P < 0.001$). The kinetics of fluorescence response of the voltage-clamped membrane region were similar between slices (Fig. 10, F and K).

To determine whether the fluorescence response to depolarization was driven by the Kv2-like puncta on the cell membrane, the fluorescence along a path containing the apparent cell membrane was selected by drawing a path connecting fluorescent puncta surrounding the dark cell body region and averaging fluorescence in a region 10-pixels (0.4-µm) wide centered on this path (Fig. 10 G, yellow line). The fluorescence intensity along the path of the ROI revealed distinct peaks corresponding to puncta (Fig. 10 H, red trace). After stepping the neuron to 0 mV, the intensity of fluorescence of a subset of puncta lessened (Fig. 10 H, black trace, peaks 1, 3, 4, 5, and 8). While the data are noisy, it is clear that even more reduction is observed in individual fluorescence puncta in brain slice (Fig. 10 I, blue line). This suggests that the voltage sensors in these functionally selected puncta are extensively activated. The EVAP model predicts only a 55% reduction of fluorescence from CHO cells stepped to 0 mV in 100 nM GxTX. The greater response of the endogenous puncta could be due to voltage sensors activating at more negative voltages in neurons than CHO cells. However, the GxTX-594 concentration within tissue may be more dilute than in the bath solution, and consequently, the sensitive fraction calculated from the EVAP model is a lower bound. Other puncta maintained or increased their brightness after depolarization (Fig. 10 H, black trace, peaks 2, 6, and 7), but it was unclear whether these voltage-insensitive puncta correspond to Kv2 proteins on the surface of the same voltage-clamped neuron. When the kinetics of fluorescence intensity decay of individual voltage-sensitive puncta were fit with Eq. 1, $k_{\Delta F}$ values were similar between puncta (Fig. 10 I), consistent with these spatially separated puncta all being on the surface of the voltage-clamped neuron. The $k_{\Delta F}$ changes measured in these puncta were similar to those predicted by the Fig. 7 model (Fig. 10 I, blue line), although the variability of these measurements was substantial. To address whether the fluorescence change at the cell membrane was driven by decreases in regions of punctate fluorescence, the punctate and nonpunctate fluorescence intensity changes were analyzed separately. The regions with fluorescence intensities above average for the path (Fig. 10 H, dotted line) were binned as one group. The above-average group, by definition, contained all punctate fluorescence. When comparing the fluorescence before and during the 0-mV step, the regions that were initially of below-average fluorescence

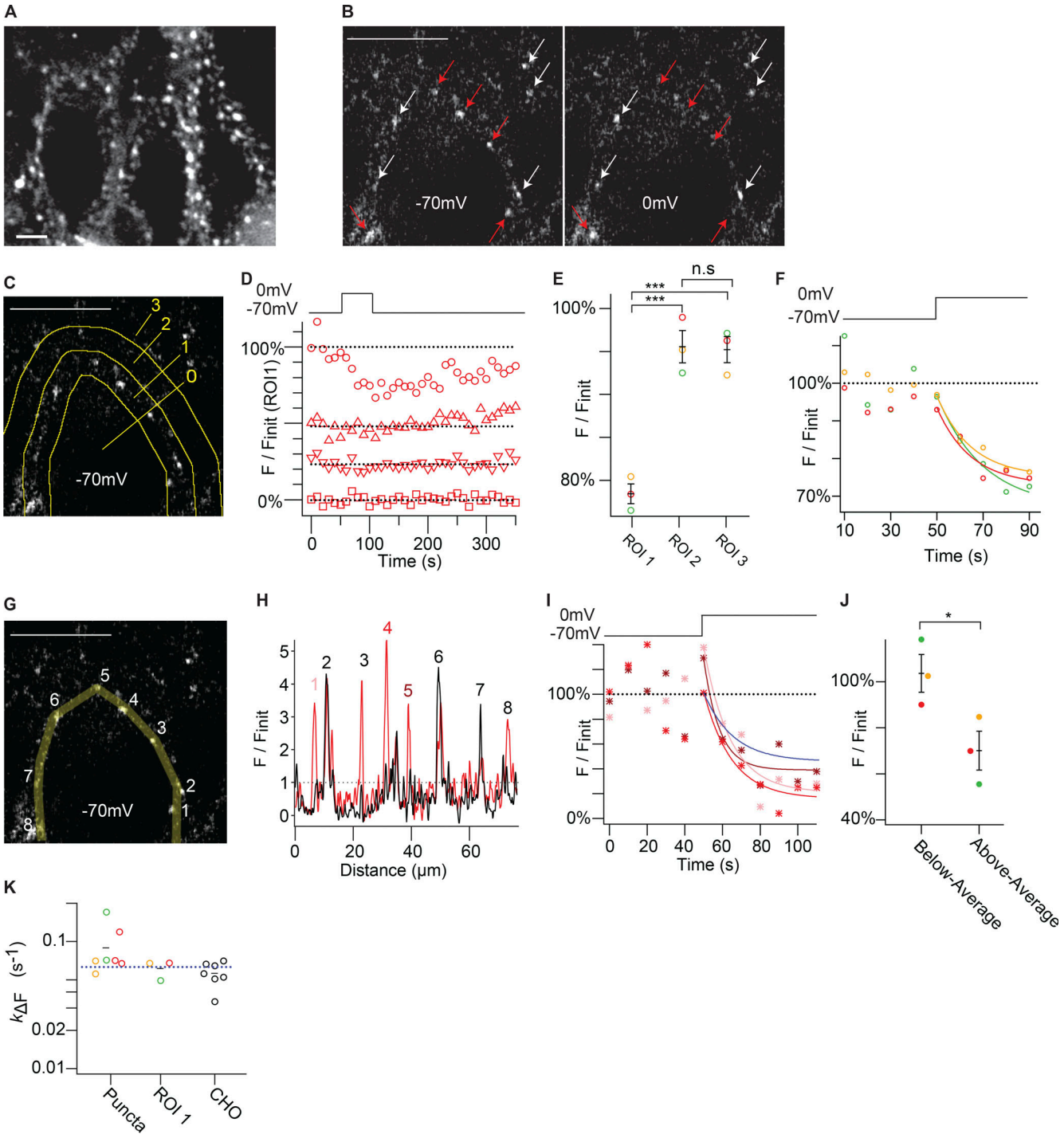

Figure 10. **GxTX-594 puncta on hippocampal CA1 neurons are sensitive to voltage stimulus. (A)** Two-photon excitation optical section from CA1 pyramidal neurons in a cultured hippocampal slice after incubation with 100 nM GxTX-594. Scale bar, 5 µm. **(B)** 594 fluorescence from a single two-photon excitation optical section before and during depolarization of a whole-cell patch-clamped neuron. Text labels of holding potential (−70 mV or 0 mV) indicate approximate position of the patch-clamp pipette. Red arrows indicate stimulus-sensitive puncta; white arrows indicate stimulus-insensitive puncta. Left panel is the average fluorescence of the three frames at −70 mV before depolarization, while the right panel is the average fluorescence of three frames after holding potential was stepped to 0 mV. Scale bar, 5 µm. Video 1 contains time-lapse images from this experiment. **(C)** ROIs used in analysis for D–F. Same slice as B. ROI 1 contains the apparent plasma membrane of the cell body of the patch-clamped neuron; it was generated by drawing a path tracing the apparent plasma membrane and then expanding to an ROI containing 15 pixels on either side of the path (1.2 µm total width). ROI 2 contains the area 15–45 pixels outside the membrane path (1.2 µm total width). RO1 3 contains the area >45 pixels outside the membrane path. ROI 0 contains the area >15 pixels inside the membrane path. Scale bar, 5 µm. **(D)** Fluorescence from each ROI shown in C. Squares represent ROI 0, circles represent ROI 1, up triangles represent ROI 2, and down triangles represent ROI 3. Background was defined as the mean fluorescence of ROI 0 during the experiment. F_{init} was defined as the mean fluorescence of ROI 1 during the first six frames, after subtraction of background. Dotted lines represent the average fluorescence of the first six frames of each ROI. The voltage protocol is shown above the graph. **(E)** Change in fluorescence during a 0-mV step for different ROIs in three hippocampal slices from three separate rats. ROIs

for each slice were defined by methods described in C. Circles represent mean fluorescence from six frames during 0-mV stimulus (F), normalized to mean fluorescence from the same ROI in six frames before stimulus (F_{init}). Circle color is consistent between ROIs for each hippocampal slice; red circles are from the slice shown in D. Black bars are arithmetic mean ± SE from three hippocampal slices. A statistical difference between ROIs was detected by ANOVA (P = 0.0003) followed by the Tukey's post hoc test, where ROI 1 versus ROI 2 (***, P < 0.001), ROI 1 versus ROI 3 (***, P < 0.001), and ROI 2 versus ROI 3 (n.s., P = 0.98). **(F)** Kinetics of fluorescence change from ROI 1 during a 0-mV step in three hippocampal slices. ROI 1 for each slice was defined by the methods described in C. Lines are monoexponential fits (Eq. 1): $k_{\Delta F}$ = 6.8 × 10^{-2} ± 2.6 × 10^{-2} s^{-1} (yellow), 6.8 × 10^{-2} ± 4.6 × 10^{-2} s^{-1} (red), and 4.9 × 10^{-2} ± 2.10^{-2} s^{-1} (green). The voltage protocol is shown above the graph. Colors of individual circles indicate the same slices as E. **(G)** ROI used in analysis for H–J. Same image as C. The shaded ROI was generated by drawing a path tracing the apparent plasma membrane and then expanding to an ROI containing 5 pixels on either side of the path (0.4 µm total width). Numbers indicate puncta that appear as peaks in H. Scale bar, 5 µm. **(H)** A plot of the fluorescence intensity along the ROI shown in G before (red trace) and during (black trace) 0-mV stimulus. Numbers above peaks correspond to puncta labeled in G. Red trace: Mean fluorescence intensity during the three frames immediately before the stimulus, normalized to mean intensity of entire ROI (black dotted line), plotted against distance along path. Black trace: Mean fluorescence intensity during three frames at 0 mV, normalized by the same F_{init} value as the red trace. **(I)** Kinetics of fluorescence change of individual puncta from G. Puncta intensity are average intensity of points extending to half maximum of each peak in H. Asterisks indicate mean fluorescence intensity of puncta 1 (pink), 4 (red), and 5 (dark red). Lines are monoexponential fits (Eq. 1): $k_{\Delta F}$ = 7.10^{-2} ± 2.9 × 10^{-2} s^{-1} (pink), 6.7 × 10^{-2} ± 2.5 × 10^{-2} s^{-1} (red), and 1.2 × 10^{-1} ± 5.6 × 10^{-2} s^{-1} (dark red). Fits to other puncta had SDs larger than $k_{\Delta F}$ values and were excluded. F_{init} was defined as the mean background-subtracted fluorescence of the puncta during the six frames before stimuli. The voltage protocol is displayed above the graph. Blue line is prediction from Scheme 1. **(J)** Comparison of fluorescence change of puncta (above average) and interpuncta (below average) regions in response to 0-mV stimulus. The regions before stimulus shown by the red line of H that had F/F_{init} ≥1 (above average) were binned separately from regions with F/F_{init} <1. The mean fluorescence of each region during 0-mV stimulus (H, black trace) was compared with the fluorescence before stimulus (H, red trace). Circles indicate values from three independent hippocampal slices; colors indicate same slices as E and F. A weak statistical difference in fluorescence was detected between interpuncta and puncta regions by Student's t test (*, P = 0.046). Black bars are arithmetic mean ± SE. **(K)** Rate of fluorescence change of GxTX-594 after a 0-mV stimulus from puncta (as in I), ROI 1 (as in F), or Kv2.1-CHO cells in 100 nM GxTX-594. Kv2.1-CHO cells were imaged at the same temperature as neurons (30°C) using neuronal intracellular solution. CHO CE solution was used for Kv2.1-CHO cell experiments. Kv2.1-CHO measurements were made by Airy disk confocal imaging. Black bars are mean ± SEM from data shown. Blue dotted line is $k_{\Delta F}$ = 6.31 × 10^{-2} s^{-1} prediction of Scheme 1. No statistical difference was detected between groups by ANOVA (P = 0.11).

maintained the same intensity (103 ± 8%); regions that were initially of above-average fluorescence decreased in intensity (70 ± 8%; Fig. 10 J). This suggests that the detectable unlabeling along the cell membrane originated in the Kv2-like puncta, not the regions of lower fluorescence intensity between them.

To determine whether the dynamics of the voltage-dependent responses of GxTX-594 fluorescence on neurons in brain slices were consistent with reversible labeling of Kv2.1, we performed experiments with Kv2.1-expressing CHO cells under similar conditions as brain slice: 100 nM GxTX-594, 30°C, Cs^+-containing patch pipette solution. The rate of fluorescence changes in Kv2.1-CHO cells was similar to neurons in brain slices and consistent with the $k_{\Delta F}$ of 0.06 s^{-1} predicted by the Fig. 7 model (Fig. 10 K). However, the data underlying of $k_{\Delta F}$ measurements were noisy, limiting our ability to detect differences.

Discussion

The molecular targeting, conformation selectivity, and spatial precision of fluorescence from GxTX-594 enable identification of where in tissue the conformational status of Kv2 voltage sensors becomes altered. However, the utility of GxTX-594 as an EVAP is limited by several factors, including emission intensity, variability between experiments, and inhibition of Kv2 proteins. We discuss the potential utility and limitations of the EVAP mechanism underlying GxTX-594.

Unique capabilities of GxTX-594

The Kv2 EVAP presented here is the only imaging method we are aware of for measuring voltage-sensitive conformational changes of a specific, endogenous protein. As GxTX binding selectively stabilizes the fully resting conformation of Kv2.1 voltage sensors (Tilley et al., 2019), reversible GxTX-594 labeling is expected to bind with highest affinity specifically to the fully resting conformation of the Kv2 voltage sensor in which the first gating charge of the Kv2 S4 segment is in the gating charge transfer center (Tao et al., 2010). Images of GxTX-594 fluorescence reveal this conformation's occurrence with subcellular spatial resolution. Importantly, the EVAP model we developed allows deconvolution of the behavior of unlabeled Kv2 proteins. This enables the subcellular locations where Kv2 voltage sensing occurs to be seen for the first time.

Electrophysiological approaches can detect the voltage-sensitive K^+ conductance of Kv2 channels. However, the majority of Kv2 proteins on cell surface membranes do not function as channels and are nonconducting (Benndorf et al., 1994; Malin and Nerbonne, 2002; O'Connell et al., 2010), and Kv2 proteins dynamically regulate cellular physiology by nonconducting functions (Antonucci et al., 2001; Singer-Lahat et al., 2007; Feinshreiber et al., 2010; Dai et al., 2012; Fox et al., 2015; Johnson et al., 2018; Kirmiz et al., 2018a, 2018b, 2019; Vierra et al., 2019). The Kv2 EVAP reports on the conformation of Kv2 voltage sensors independently from ion conductance, enabling the study of voltage sensor involvement in Kv2's nonconducting physiological functions. We present this EVAP as a prototype molecular probe for imaging voltage sensing by endogenous proteins in tissue with molecular specificity.

Here, during our initial testing of GxTX-594, we observed that the majority of Kv2 protein detected at discrete individual clusters was voltage sensitive. While it may not be surprising to find that voltage-gated ion channel proteins are voltage sensitive, the voltage sensors of surface-expressed proteins can be immobilized. For example, gating charge of the L-type Ca^{2+} channel Cav1.2 is immobilized until it is bound by an intracellular protein (Turner et al., 2020). Kv2.1 channel function is extensively regulated by neurons. In rat CA1 neurons, the clustered Kv2 channels are proposed to be nonconducting (Fox et al., 2013b). Our results show that clustered Kv2 proteins in rat

CA1 neurons remain voltage sensitive. Interestingly, when Kv2.1 is expressed in CHO cells, a fraction of the GxTX-594 fluorescence is voltage insensitive (Fig. 6 C). This observation is consistent with voltage sensor immobilization of some surface-expressed Kv2.1 protein, although it could be due to intracellular Kv2.1–GxTX-594 proteins that appear to be at the cell surface.

We used images of GxTX-594 fluorescence to measure the coupling between endogenous Kv2 proteins and membrane potential at specific, subcellular anatomical locations. Similarly, GxTX-594 imaging should detect changes of voltage sensor status when Kv2 proteins become engaged or disengaged from nonconducting functions, such as formation of plasma membrane–endoplasmic reticulum junctions (Antonucci et al., 2001; Fox et al., 2015; Kirmiz et al., 2018a), regulation of exocytosis (Singer-Lahat et al., 2007; Feinshreiber et al., 2010), regulation of insulin secretion (Dai et al., 2012), interaction with kinases, phosphatases, and SUMOylases (Misonou et al., 2004; Park et al., 2006; Dai et al., 2009; Cerda and Trimmer, 2011; McCord and Aizenman, 2013), formation of specialized subcellular calcium signaling domains (Vierra et al., 2019), and interactions with astrocytic end feet (Du et al., 1998). GxTX-594 could potentially reveal conformational changes in organs throughout the body where Kv2 proteins are expressed, which include muscle, thymus, spleen, kidney, adrenal gland, pancreas, lung, and reproductive organs (Bocksteins, 2016).

Limitations of GxTX-594

There are important limitations to the GxTX-594 approach and of the underlying EVAP mechanism generally. We discuss several limitations that are worth considering in the design of any studies with GxTX-594.

GxTX-594 labeling is slower than channel gating

The kinetics of reversible GxTX-594 labeling are limited to measuring changes in Kv2 activity on a time scale of tens of seconds. While the temporal resolution of GxTX-594 is compatible with live imaging and electrophysiology experiments, labeling kinetics do not provide sufficient time resolution to distinguish fast electrical signaling events. The response time of GxTX-594 is far slower than the kinetics of Kv2 conformational change, limiting measurements to the probability, averaged over time, that voltage sensors are resting or active. It is worth noting that the probability of a conformation's occurrence can be a valuable measure and is the ultimate quantitation of many biophysical studies of ion channels (e.g., open probability, steady-state conductance, and gating charge–voltage relation).

GxTX-594 dynamics are altered in confined extracellular spaces

The kinetics of GxTX-594 dynamics varied within different regions of the same CHO cell (Fig. S4). The location dependence of $k_{\Delta F}$ was more pronounced during GxTX-594 labeling at −80 mV than unlabeling at +40 mV, and such a difference can be explained by the distinct voltage-dependent affinities of Kv2.1 for GxTX-594. We suspect that the more extreme location dependence at −80 mV is due to a high density of Kv2.1 binding sites in the restricted extracellular space between the cell membrane and glass coverslip, such that GxTX-594 is depleted from solution by binding Kv2.1 before reaching the center of the cell. After unbinding at +40 mV, Kv2.1 proteins are in activated, low-affinity conformations, which are unlikely to rebind GxTX-594 and, thus, do not slow their diffusion across the cell surface. The space extracellular to Kv2.1 channel clusters of hippocampal and cortical interneurons is restricted by astrocytic end feet, which create an extracellular cleft only a few nanometers wide (Du et al., 1998). Such restricted spaces may slow the kinetics of labeling in the hippocampal slices (Fig. 10).

GxTX-594 dynamics are variable between CHO cells

The variability of GxTX-594 response rates and amplitudes between CHO cells limited the precision of results. Some of this variability is expected from technical imprecisions: Fits of $k_{\Delta F}$ where the final value of the relaxation was poorly determined by the data, small changes due to variations of room temperature, photobleaching, and other potential sources. However, we noticed that results were more consistent between stimuli of the same cell, and the variability was greatest between cells (Fig. 6, D and E; and Fig. 8, C and D). We suspect that cell-to-cell differences in Kv2.1 conformational equilibria are responsible for much of the variability in GxTX-594 response. The Kv2.1 conductance–voltage relation is regulated by many cellular pathways, including kinases, phosphatases, and SUMOylases (Misonou et al., 2004; Park et al., 2006; Dai et al., 2009; Cerda and Trimmer, 2011; McCord and Aizenman, 2013). Large cell-to-cell variation in Kv2.1 conductance–voltage and gating charge–voltage relations have been reported in CHO cells by our group and others (McCrossan et al., 2009; Tilley et al., 2014; Kang et al., 2019; Tilley et al., 2019). In this study, when we predicted the voltage sensor $V_{1/2}$ of Kv2.1 from electrophysiology, we observed a 6.4-mV SD with a range of 19 mV, and this variance appeared to be exacerbated by GxTX-594 having a 9.7-mV SD and range of 36 mV (Fig. 1 E). As EVAP dynamics and the *GV* are both determined by voltage sensor activation, variability in the GxTX-594 response is expected. The hypothesis that cell-to-cell variation in fluorescence dynamics is due to the inherent variability of Kv2.1 voltage sensor activation could be more definitively tested by identifying whether a correlation exists between the $V_{1/2}$ of the *QV* and fluorescence–voltage relationship from individual cells labeled with GxTX-594. While we have not attempted this, the structure of the variance in GxTX-594 fluorescence–voltage relationships is informative. The fluorescence–voltage relationships compiled from many cells become more variable near the midpoint of relevant voltage sensor movements. The response amplitude F/F_{init} (Fig. 6 D) is determined by unlabeled voltage sensor activation and appears most variable near the $V_{1/2}$ of the unlabeled *QV* relation (−32 mV; Tilley et al., 2019). The response kinetics $k_{\Delta F}$ are determined by activation of voltage sensors, which have GxTX-594 bound and appear to become increasingly variable at voltages higher than −20 mV (Fig. 6 E, bottom panel). Despite this variability, the $V_{1/2}$ and z from the Boltzmann fit of the $k_{\Delta F}$–voltage relationship from many cells were remarkably close to the *QV* of the GxTX–Kv2.1 complex, with a $V_{1/2}$ and z that differ by 3.3 mV and 0.07 e_0, respectively (Tilley et al., 2019).

Another possibility is that variability in surface membrane composition undergirds the variability of the GxTX-594 response.

GxTX affinities are influenced by the dynamically changing complement of lipids in the plasma membrane lipid composition. Lipids bind to the voltage-sensing domain near the GxTX binding site (Milescu et al., 2009; Gupta et al., 2015). Sphingomyelinase D treatment, which alters the membrane composition by converting sphingomyelin to ceramide-1-phosphate, has been shown to enhance GxTX affinity for Kv2.1 fourfold (Milescu et al., 2009). Voltage activation of Kv2.1 is also affected by sphingomyelinase treatments. While variation in lipid composition is expected to cause variation in GxTX-594 dynamics, we do not know the degree to which the lipid composition varies between the Kv2.1-CHO cells in our studies.

Fluorescence intensity

Optical noise limits interpretation of EVAP imaging. While the GxTX-594 signal from CA1 neurons was sufficient to identify voltage sensing of endogenous Kv2 protein, fluorescence signal-to-noise issues limit interpretation with the EVAP model. This signal-to-noise ratio is influenced by the density of EVAP binding sites, the fluorescence intensity from each binding site, characteristics of the imaging system, and background fluorescence from unbound EVAP or other sources. As the concentration of fluorophore is lowered, background fluorescence from unbound EVAP will decrease, and the percentage of labeled binding sites will decrease. However, ΔF after voltage sensor activation remains similar, as does $k_{\Delta F}$ (Fig. 7). Due to this dynamic, the minimum concentration of EVAP that is detectable is expected to be determined by the background fluorescence and the density of EVAP binding sites. Here, we see labeling of Kv2.1-CHO cells with 1 nM GxTX-594 (Fig. 2), and previously, we found a robust fluorescence–voltage response in 1 nM GxTX-550 (Tilley et al., 2014). in each case, <10% of resting voltage sensors are bound by the EVAPs. In theory, fluorescence measurements from a single EVAP molecule immobilized by binding to a single-voltage sensor could be informative, as fluorescence from a single binding site is eliminated altogether after unbinding and diffusion away. If the EVAP imaging method does not have single-molecule resolution, the density of EVAP binding sites can limit the signal to noise.

CA1 hippocampal neurons express Kv2 proteins at a density typical of central neurons (Misonou et al., 2004; Vacher et al., 2008; Speca et al., 2014), and we expect that GxTX-594 imaging will have similar signal-to-noise characteristics in most brain regions. Improved signal to noise would be expected from such cells that express higher densities of Kv2 proteins, such as neurons of the subiculum, or the inner segment of photoreceptors (Maletic-Savatic et al., 1995; Gayet-Primo et al., 2018). Kv2 proteins are also expressed by many other cell types throughout the body (Bocksteins, 2016), where GxTX-594–labeling techniques may reveal Kv2 activity, if protein densities are sufficient.

GxTX-594 inhibits Kv2 proteins

GxTX-based probes inhibit the Kv2 proteins they label by stabilizing the resting conformation of Kv2 voltage sensors. The Kv2.1–GxTX-594 complex does not open to conduct K^+ ions in the physiological voltage range (Fig. 1). Thus, GxTX-594 depletes the population of Kv2 proteins responding normally to physiological stimuli, which could alter Kv2 signaling. The concentration of an EVAP can be lowered such that only an inconsequential minority of proteins are bound, with the trade-off being dimmer fluorescence. With a related probe, we explored the impact of decreasing concentration on fluorescence response of a GxTX-based EVAP and saw substantial fluorescence responses to voltage while inhibiting only ∼10% of Kv2.1 current (Tilley et al., 2014). Here, we demonstrate that lower concentration and physiological stimuli are not always required for scientifically meaningful implementation of an EVAP. Even when GxTX-594 inhibits most Kv2 proteins, the behavior of unlabeled Kv2 proteins can be calculated using the EVAP model we have developed. Of course, the electrical feedback within cells will be altered by such protocols.

The EVAP model is oversimplified

Another limitation of the analysis developed here is that the model of Kv2 voltage sensor conformational change is an oversimplification. The gating dynamics of Kv2 channels are more complex than our model (Islas and Sigworth, 1999; Scholle et al., 2004; Jara-Oseguera et al., 2011; Tilley et al., 2019). Under some conditions, the assumption of voltage sensor independence will limit the model's predictive power. With a related tarantula toxin, Hanatoxin, the concentration dependence for inhibition of Kv2.1 charge movement was consistent with independent binding to each voltage sensor inhibiting ∼25% of the total gating charge movement (Lee et al., 2003). This result suggests that the simplifying assumption of voltage sensor independence is reasonable. Additionally, the model of GxTX-594–reversible labeling developed here assumes that voltage sensors are in continuous equilibrium. These deviations from equilibrium likely explain the deviation of the model from the data in response to high-frequency voltage steps (Fig. 8, C and D). This model could be further tested with a Kv2 mutant, which shifts channel gating without interfering with GxTX-594 binding.

Conformation-selective probes reveal conformational changes of endogenous proteins

Measurements of dynamic reversible labeling by a conformation-selective probe such as GxTX-594 can enable deduction of how unlabeled proteins behave. This is perhaps counterintuitive because GxTX inhibits voltage sensor movement of the Kv2 protein it binds, and thus, only bound proteins generate optical signals. This approach is analogous to calcium imaging experiments, which have been spectacularly informative about physiological calcium signaling (Yang and Yuste, 2017), despite the fact that no optical signals originate from the physiologically relevant free Ca^{2+} but only from Ca^{2+} that is chelated by a dye. In all such experiments, fluorescence from Ca^{2+}-bound dyes is deconvolved using the statistical thermodynamics of Ca^{2+} binding to calculate free Ca^{2+} (Adams, 2010). Similarly, GxTX-based probes dynamically bind to unlabeled Kv2 proteins, and the binding rate depends on the probability that unlabeled voltage sensors are in a resting conformation (Fig. 7). Thus, the conformations of unlabeled Kv2 proteins influence the dynamics of labeling with GxTX-based

probes. Consequently, the dynamics of labeling reveal the conformations of unlabeled Kv2 proteins.

Deployment of GxTX-594 to report conformational changes of endogenous proteins demonstrates that conformation-selective ligands can be used to image occurrence of the conformations they bind to. The same principles of action apply to any conformation-selective labeling reagent, suggesting that probes for conformational changes of many different proteins could be developed. Probes could conceivably be developed from the many other voltage sensor toxins or other gating modifiers that act by a similar mechanism as GxTX yet target the voltage sensors of different ion channel proteins (McDonough et al., 1997; Sack et al., 2004; Catterall et al., 2007; Swartz, 2007; Schmalhofer et al., 2008; Peretz et al., 2010; McCormack et al., 2013; Ahuja et al., 2015; Dockendorff et al., 2018; Zhang et al., 2018). Conformation-selective binders have been engineered for a variety of other proteins, and methods to quantify conformational changes from their fluorescence are needed. For example, fluorescently labeled conformation-selective binders have revealed that endocytosed GPCRs continue to remain in a physiologically activated conformation (Irannejad et al., 2013; Tsvetanova et al., 2015; Eichel and von Zastrow, 2018). A means to determine the conformational equilibria of GPCRs from fluorescence images has not yet been developed. We suggest that the statistical thermodynamic framework developed here could provide a starting point for more quantitative interpretation of other conformation-selective molecular probes.

Acknowledgments

Christopher J. Lingle served as editor.

We thank Jim Trimmer (University of California, Davis) for numerous discussions and constructive critical reading of an early version of the manuscript. We thank Georgeann Sack (Afferent LLC) for critical reading, editing, and feedback.

This research was supported by National Institutes of Health grants R01NS096317 (to J.T. Sack and B.E. Cohen), U01NS090581 (to J.T. Sack), R21EY026449 (to J.T. Sack), R01NS062736 (to K. Zito), U01NS103571 (to K. Zito), T32GM007377 (to R.J. Sepela), University of California, Davis New Research Initiative award (to J.T. Sack) and American Heart Association grant 17POST33670698 (to P. Thapa). GxTX variants were synthesized at the Molecular Foundry, supported by the Director, Office of Science, Office of Basic Energy Sciences, Division of Materials Sciences and Engineering, U.S. Department of Energy under contract DE-AC02-05CH11231.

The authors declare no competing financial interests.

Author contributions: P. Thapa: Conceptualization, formal analysis, investigation, methodology, visualization, writing-original draft, writing-reviewing and editing. R. Stewart: Conceptualization, formal analysis, investigation, methodology, visualization, writing-original draft, writing-reviewing and editing. R.J. Sepela: Conceptualization, formal analysis, investigation, methodology, visualization, writing-original draft, writing-reviewing and editing. O. Vivas: Investigation, methodology, writing-reviewing and editing. L.K. Parajuli: Investigation, methodology, writing-reviewing and editing. M. Lillya: Conceptualization, formal analysis, investigation, methodology, visualization, writing-reviewing and editing. S. Fletcher-Taylor: Investigation, methodology, writing-reviewing and editing. B.E. Cohen: Conceptualization, funding acquisition, project administration, supervision, writing-reviewing and editing. K. Zito: Conceptualization, funding acquisition, investigation, methodology, project administration, supervision, writing-original draft, writing-reviewing and editing. J.T. Sack: Conceptualization, formal analysis, funding acquisition, investigation, methodology, project administration, supervision, visualization, writing-original draft, writing-reviewing and editing.

Submitted: 3 January 2021
Accepted: 3 September 2021

References

Adams, S.R. 2010. How calcium indicators work. *Cold Spring Harb. Protoc.* 2010:top70. https://doi.org/10.1101/pdb.top70

Aggarwal, S.K., and R. MacKinnon. 1996. Contribution of the S4 segment to gating charge in the Shaker K^+ channel. *Neuron.* 16:1169–1177. https://doi.org/10.1016/S0896-6273(00)80143-9

Ahuja, S., S. Mukund, L. Deng, K. Khakh, E. Chang, H. Ho, S. Shriver, C. Young, S. Lin, J.P. Johnson Jr., et al. 2015. Structural basis of Nav1.7 inhibition by an isoform-selective small-molecule antagonist. *Science.* 350:aac5464. https://doi.org/10.1126/science.aac5464

An, W.F., M.R. Bowlby, M. Betty, J. Cao, H.P. Ling, G. Mendoza, J.W. Hinson, K.I. Mattsson, B.W. Strassle, J.S. Trimmer, and K.J. Rhodes. 2000. Modulation of A-type potassium channels by a family of calcium sensors. *Nature.* 403:553–556. https://doi.org/10.1038/35000592

Antonucci, D.E., S.T. Lim, S. Vassanelli, and J.S. Trimmer. 2001. Dynamic localization and clustering of dendritic Kv2.1 voltage-dependent potassium channels in developing hippocampal neurons. *Neuroscience.* 108:69–81. https://doi.org/10.1016/S0306-4522(01)00476-6

Armstrong, C.M., and F. Bezanilla. 1973. Currents related to movement of the gating particles of the sodium channels. *Nature.* 242:459–461. https://doi.org/10.1038/242459a0

Benndorf, K., R. Koopmann, C. Lorra, and O. Pongs. 1994. Gating and conductance properties of a human delayed rectifier K^+ channel expressed in frog oocytes. *J. Physiol.* 477:1–14. https://doi.org/10.1113/jphysiol.1994.sp020166

Bezanilla, F. 2008. How membrane proteins sense voltage. *Nat. Rev. Mol. Cell Biol.* 9:323–332. https://doi.org/10.1038/nrm2376

Bezanilla, F. 2018. Gating currents. *J. Gen. Physiol.* 150:911–932. https://doi.org/10.1085/jgp.201812090

Bocksteins, E. 2016. Kv5, Kv6, Kv8, and Kv9 subunits: No simple silent bystanders. *J. Gen. Physiol.* 147:105–125. https://doi.org/10.1085/jgp.201511507

Bolte, S., and F.P. Cordelières. 2006. A guided tour into subcellular colocalization analysis in light microscopy. *J. Microsc.* 224:213–232. https://doi.org/10.1111/j.1365-2818.2006.01706.x

Catterall, W.A., S. Cestèle, V. Yarov-Yarovoy, F.H. Yu, K. Konoki, and T. Scheuer. 2007. Voltage-gated ion channels and gating modifier toxins. *Toxicon.* 49:124–141. https://doi.org/10.1016/j.toxicon.2006.09.022

Cerda, O., and J.S. Trimmer. 2011. Activity-dependent phosphorylation of neuronal Kv2.1 potassium channels by CDK5. *J. Biol. Chem.* 286:28738–28748. https://doi.org/10.1074/jbc.M111.251942

Dai, X.Q., J. Kolic, P. Marchi, S. Sipione, and P.E. Macdonald. 2009. SUMOylation regulates Kv2.1 and modulates pancreatic beta-cell excitability. *J. Cell Sci.* 122:775–779. https://doi.org/10.1242/jcs.036632

Dai, X.Q., J.E. Manning Fox, D. Chikvashvili, M. Casimir, G. Plummer, C. Hajmrle, A.F. Spigelman, T. Kin, D. Singer-Lahat, Y. Kang, et al. 2012. The voltage-dependent potassium channel subunit Kv2.1 regulates insulin secretion from rodent and human islets independently of its electrical function. *Diabetologia.* 55:1709–1720. https://doi.org/10.1007/s00125-012-2512-6

Deutsch, E., A.V. Weigel, E.J. Akin, P. Fox, G. Hansen, C.J. Haberkorn, R. Loftus, D. Krapf, and M.M. Tamkun. 2012. Kv2.1 cell surface clusters are insertion platforms for ion channel delivery to the plasma membrane. *Mol. Biol. Cell.* 23:2917–2929. https://doi.org/10.1091/mbc.e12-01-0047

Dockendorff, C., D.M. Gandhi, I.H. Kimball, K.S. Eum, R. Rusinova, H.I. Ingólfsson, R. Kapoor, T. Peyear, M.W. Dodge, S.F. Martin, et al. 2018.

Synthetic analogues of the snail toxin 6-bromo-2-mercaptotryptamine Dimer (BrMT) reveal that lipid bilayer perturbation does not underlie its modulation of voltage-gated potassium channels. *Biochemistry*. 57: 2733–2743. https://doi.org/10.1021/acs.biochem.8b00292

Du, J., J.H. Tao-Cheng, P. Zerfas, and C.J. McBain. 1998. The K^+ channel, Kv2.1, is apposed to astrocytic processes and is associated with inhibitory postsynaptic membranes in hippocampal and cortical principal neurons and inhibitory interneurons. *Neuroscience*. 84:37–48. https://doi.org/10.1016/S0306-4522(97)00519-8

Du, J., L.L. Haak, E. Phillips-Tansey, J.T. Russell, and C.J. McBain. 2000. Frequency-dependent regulation of rat hippocampal somato-dendritic excitability by the K^+ channel subunit Kv2.1. *J. Physiol.* 522:19–31. https://doi.org/10.1111/j.1469-7793.2000.t01-2-00019.xm

Eichel, K., and M. von Zastrow. 2018. Subcellular organization of GPCR signaling. *Trends Pharmacol. Sci.* 39:200–208. https://doi.org/10.1016/j.tips.2017.11.009

Feinshreiber, L., D. Singer-Lahat, R. Friedrich, U. Matti, A. Sheinin, O. Yizhar, R. Nachman, D. Chikvashvili, J. Rettig, U. Ashery, and I. Lotan. 2010. Non-conducting function of the Kv2.1 channel enables it to recruit vesicles for release in neuroendocrine and nerve cells. *J. Cell Sci.* 123: 1940–1947. https://doi.org/10.1242/jcs.063719

Fletcher-Taylor, S., P. Thapa, R.J. Sepela, R. Kaakati, V. Yarov-Yarovoy, J.T. Sack, and B.E. Cohen. 2020. Distinguishing potassium channel resting state conformations in live cells with environment-sensitive fluorescence. *ACS Chem. Neurosci.* 11:2316–2326. https://doi.org/10.1021/acschemneuro.0c00276

Fox, P.D., C.J. Haberkorn, A.V. Weigel, J.L. Higgins, E.J. Akin, M.J. Kennedy, D. Krapf, and M.M. Tamkun. 2013a. Plasma membrane domains enriched in cortical endoplasmic reticulum function as membrane protein trafficking hubs. *Mol. Biol. Cell.* 24:2703–2713. https://doi.org/10.1091/mbc.e12-12-0895

Fox, P.D., R.J. Loftus, and M.M. Tamkun. 2013b. Regulation of Kv2.1 K^+ conductance by cell surface channel density. *J. Neurosci.* 33:1259–1270. https://doi.org/10.1523/JNEUROSCI.3008-12.2013

Fox, P.D., C.J. Haberkorn, E.J. Akin, P.J. Seel, D. Krapf, and M.M. Tamkun. 2015. Induction of stable ER-plasma-membrane junctions by Kv2.1 potassium channels. *J. Cell Sci.* 128:2096–2105. https://doi.org/10.1242/jcs.166009

Frech, G.C., A.M. VanDongen, G. Schuster, A.M. Brown, and R.H. Joho. 1989. A novel potassium channel with delayed rectifier properties isolated from rat brain by expression cloning. *Nature*. 340:642–645. https://doi.org/10.1038/340642a0

Gayet-Primo, J., D.B. Yaeger, R.A. Khanjian, and T. Puthussery. 2018. Heteromeric $K_V2/K_V8.2$ channels mediate delayed rectifier potassium currents in primate photoreceptors. *J. Neurosci.* 38:3414–3427. https://doi.org/10.1523/JNEUROSCI.2440-17.2018

Gordon, E., T.K. Roepke, and G.W. Abbott. 2006. Endogenous KCNE subunits govern Kv2.1 K^+ channel activation kinetics in Xenopus oocyte studies. *Biophys. J.* 90:1223–1231. https://doi.org/10.1529/biophysj.105.072504

Gupta, K., M. Zamanian, C. Bae, M. Milescu, D. Krepkiy, D.C. Tilley, J.T. Sack, V. Yarov-Yarovoy, J.I. Kim, and K.J. Swartz. 2015. Tarantula toxins use common surfaces for interacting with Kv and ASIC ion channels. *eLife*. 4:e06774. https://doi.org/10.7554/eLife.06774

Herrington, J., Y.P. Zhou, R.M. Bugianesi, P.M. Dulski, Y. Feng, V.A. Warren, M.M. Smith, M.G. Kohler, V.M. Garsky, M. Sanchez, et al. 2006. Blockers of the delayed-rectifier potassium current in pancreatic β-cells enhance glucose-dependent insulin secretion. *Diabetes*. 55:1034–1042. https://doi.org/10.2337/diabetes.55.04.06.db05-0788

Irannejad, R., J.C. Tomshine, J.R. Tomshine, M. Chevalier, J.P. Mahoney, J. Steyaert, S.G. Rasmussen, R.K. Sunahara, H. El-Samad, B. Huang, and M. von Zastrow. 2013. Conformational biosensors reveal GPCR signalling from endosomes. *Nature*. 495:534–538. https://doi.org/10.1038/nature12000

Islas, L.D., and F.J. Sigworth. 1999. Voltage sensitivity and gating charge in Shaker and Shab family potassium channels. *J. Gen. Physiol.* 114:723–742. https://doi.org/10.1085/jgp.114.5.723

Jara-Oseguera, A., I.G. Ishida, G.E. Rangel-Yescas, N. Espinosa-Jalapa, J.A. Pérez-Guzmán, D. Elías-Viñas, R. Le Lagadec, T. Rosenbaum, and L.D. Islas. 2011. Uncoupling charge movement from channel opening in voltage-gated potassium channels by ruthenium complexes. *J. Biol. Chem.* 286:16414–16425. https://doi.org/10.1074/jbc.M110.198010

Johnson, B., A.N. Leek, L. Solé, E.E. Maverick, T.P. Levine, and M.M. Tamkun. 2018. Kv2 potassium channels form endoplasmic reticulum/plasma membrane junctions via interaction with VAPA and VAPB. *Proc. Natl. Acad. Sci. USA*. 115:E7331–E7340. https://doi.org/10.1073/pnas.1805757115

Kaczmarek, L.K. 2006. Non-conducting functions of voltage-gated ion channels. *Nat. Rev. Neurosci.* 7:761–771. https://doi.org/10.1038/nrn1988

Kang, S.K., C.G. Vanoye, S.N. Misra, D.M. Echevarria, J.D. Calhoun, J.B. O'Connor, K.L. Fabre, D. McKnight, L. Demmer, P. Goldenberg, et al. 2019. Spectrum of K_V 2.1 dysfunction in KCNB1-associated neurodevelopmental disorders. *Ann. Neurol.* 86:899–912. https://doi.org/10.1002/ana.25607

Kirmiz, M., S. Palacio, P. Thapa, A.N. King, J.T. Sack, and J.S. Trimmer. 2018a. Remodeling neuronal ER-PM junctions is a conserved nonconducting function of Kv2 plasma membrane ion channels. *Mol. Biol. Cell.* 29: 2410–2432. https://doi.org/10.1091/mbc.E18-05-0337

Kirmiz, M., N.C. Vierra, S. Palacio, and J.S. Trimmer. 2018b. Identification of VAPA and VAPB as Kv2 channel-interacting proteins defining endoplasmic reticulum-plasma membrane junctions in mammalian brain neurons. *J. Neurosci.* 38:7562–7584. https://doi.org/10.1523/JNEUROSCI.0893-18.2018

Kirmiz, M., T.E. Gillies, E.J. Dickson, and J.S. Trimmer. 2019. Neuronal ER-plasma membrane junctions organized by Kv2-VAP pairing recruit Nir proteins and affect phosphoinositide homeostasis. *J. Biol. Chem.* 294: 17735–17757. https://doi.org/10.1074/jbc.RA119.007635

Lee, H.C., J.M. Wang, and K.J. Swartz. 2003. Interaction between extracellular Hanatoxin and the resting conformation of the voltage-sensor paddle in Kv channels. *Neuron*. 40:527–536. https://doi.org/10.1016/S0896-6273(03)00636-6

Legant, W.R., L. Shao, J.B. Grimm, T.A. Brown, D.E. Milkie, B.B. Avants, L.D. Lavis, and E. Betzig. 2016. High-density three-dimensional localization microscopy across large volumes. *Nat. Methods*. 13:359–365. https://doi.org/10.1038/nmeth.3797

Lewis, G.N. 1925. A new principle of equilibrium. *Proc. Natl. Acad. Sci. USA*. 11: 179–183. https://doi.org/10.1073/pnas.11.3.179

Li, H., W. Guo, H. Xu, R. Hood, A.T. Benedict, and J.M. Nerbonne. 2001. Functional expression of a GFP-tagged Kv1.5 alpha-subunit in mouse ventricle. *Am. J. Physiol. Heart Circ. Physiol.* 281:H1955–H1967. https://doi.org/10.1152/ajpheart.2001.281.5.H1955

Lin, M.Z., and M.J. Schnitzer. 2016. Genetically encoded indicators of neuronal activity. *Nat. Neurosci.* 19:1142–1153. https://doi.org/10.1038/nn.4359

Liu, P.W., and B.P. Bean. 2014. Kv2 channel regulation of action potential repolarization and firing patterns in superior cervical ganglion neurons and hippocampal CA1 pyramidal neurons. *J. Neurosci.* 34:4991–5002. https://doi.org/10.1523/JNEUROSCI.1925-13.2014

Long, S.B., E.B. Campbell, and R. Mackinnon. 2005. Voltage sensor of Kv1.2: structural basis of electromechanical coupling. *Science*. 309:903–908. https://doi.org/10.1126/science.1116270

Long, S.B., X. Tao, E.B. Campbell, and R. MacKinnon. 2007. Atomic structure of a voltage-dependent K^+ channel in a lipid membrane-like environment. *Nature*. 450:376–382. https://doi.org/10.1038/nature06265

MacDonald, P.E., A.M. Salapatek, and M.B. Wheeler. 2003. Temperature and redox state dependence of native Kv2.1 currents in rat pancreatic beta-cells. *J. Physiol.* 546:647–653. https://doi.org/10.1113/jphysiol.2002.035709

Maletic-Savatic, M., N.J. Lenn, and J.S. Trimmer. 1995. Differential spatiotemporal expression of K^+ channel polypeptides in rat hippocampal neurons developing in situ and in vitro. *J. Neurosci.* 15:3840–3851. https://doi.org/10.1523/JNEUROSCI.15-05-03840.1995

Malin, S.A., and J.M. Nerbonne. 2002. Delayed rectifier K^+ currents, IK, are encoded by Kv2 alpha-subunits and regulate tonic firing in mammalian sympathetic neurons. *J. Neurosci.* 22:10094–10105. https://doi.org/10.1523/JNEUROSCI.22-23-10094.2002

McCord, M.C., and E. Aizenman. 2013. Convergent Ca^{2+} and Zn^{2+} signaling regulates apoptotic Kv2.1 K^+ currents. *Proc. Natl. Acad. Sci. USA*. 110: 13988–13993. https://doi.org/10.1073/pnas.1306238110

McCormack, K., S. Santos, M.L. Chapman, D.S. Krafte, B.E. Marron, C.W. West, M.J. Krambis, B.M. Antonio, S.G. Zellmer, D. Printzenhoff, et al. 2013. Voltage sensor interaction site for selective small molecule inhibitors of voltage-gated sodium channels. *Proc. Natl. Acad. Sci. USA*. 110: E2724–E2732. https://doi.org/10.1073/pnas.1220844110

McCrossan, Z.A., T.K. Roepke, A. Lewis, G. Panaghie, and G.W. Abbott. 2009. Regulation of the Kv2.1 potassium channel by MinK and MiRP1. *J. Membr. Biol.* 228:1–14. https://doi.org/10.1007/s00232-009-9154-8

McDonough, S.I., I.M. Mintz, and B.P. Bean. 1997. Alteration of P-type calcium channel gating by the spider toxin omega-Aga-IVA. *Biophys. J.* 72: 2117–2128. https://doi.org/10.1016/S0006-3495(97)78854-4

Milescu, M., F. Bosmans, S. Lee, A.A. Alabi, J.I. Kim, and K.J. Swartz. 2009. Interactions between lipids and voltage sensor paddles detected with

tarantula toxins. *Nat. Struct. Mol. Biol.* 16:1080–1085. https://doi.org/10.1038/nsmb.1679

Misonou, H., D.P. Mohapatra, E.W. Park, V. Leung, D. Zhen, K. Misonou, A.E. Anderson, and J.S. Trimmer. 2004. Regulation of ion channel localization and phosphorylation by neuronal activity. *Nat. Neurosci.* 7:711–718. https://doi.org/10.1038/nn1260

Misonou, H., D.P. Mohapatra, M. Menegola, and J.S. Trimmer. 2005. Calcium- and metabolic state-dependent modulation of the voltage-dependent Kv2.1 channel regulates neuronal excitability in response to ischemia. *J. Neurosci.* 25:11184–11193. https://doi.org/10.1523/JNEUROSCI.3370-05.2005

Murakoshi, H., G. Shi, R.H. Scannevin, and J.S. Trimmer. 1997. Phosphorylation of the Kv2.1 K^+ channel alters voltage-dependent activation. *Mol. Pharmacol.* 52:821–828. https://doi.org/10.1124/mol.52.5.821

O'Connell, K.M., R. Loftus, and M.M. Tamkun. 2010. Localization-dependent activity of the Kv2.1 delayed-rectifier K^+ channel. *Proc. Natl. Acad. Sci. USA.* 107:12351–12356. https://doi.org/10.1073/pnas.1003028107

Opitz-Araya, X., and A. Barria. 2011. Organotypic hippocampal slice cultures. *J. Vis. Exp.* (48):2462.

Park, K.S., D.P. Mohapatra, H. Misonou, and J.S. Trimmer. 2006. Graded regulation of the Kv2.1 potassium channel by variable phosphorylation. *Science.* 313:976–979. https://doi.org/10.1126/science.1124254

Peltola, M.A., J. Kuja-Panula, S.E. Lauri, T. Taira, and H. Rauvala. 2011. AMIGO is an auxiliary subunit of the Kv2.1 potassium channel. *EMBO Rep.* 12:1293–1299. https://doi.org/10.1038/embor.2011.204

Peretz, A., L. Pell, Y. Gofman, Y. Haitin, L. Shamgar, E. Patrich, P. Kornilov, O. Gourgy-Hacohen, N. Ben-Tal, and B. Attali. 2010. Targeting the voltage sensor of Kv7.2 voltage-gated K^+ channels with a new gating-modifier. *Proc. Natl. Acad. Sci. USA.* 107:15637–15642. https://doi.org/10.1073/pnas.0911294107

Plant, L.D., E.J. Dowdell, I.S. Dementieva, J.D. Marks, and S.A. Goldstein. 2011. SUMO modification of cell surface Kv2.1 potassium channels regulates the activity of rat hippocampal neurons. *J. Gen. Physiol.* 137:441–454. https://doi.org/10.1085/jgp.201110604

Pologruto, T.A., B.L. Sabatini, and K. Svoboda. 2003. ScanImage: flexible software for operating laser scanning microscopes. *Biomed. Eng. Online.* 2:13. https://doi.org/10.1186/1475-925X-2-13

Ramu, Y., Y. Xu, and Z. Lu. 2006. Enzymatic activation of voltage-gated potassium channels. *Nature.* 442:696–699. https://doi.org/10.1038/nature04880

Sack, J.T., R.W. Aldrich, and W.F. Gilly. 2004. A gastropod toxin selectively slows early transitions in the Shaker K channel's activation pathway. *J. Gen. Physiol.* 123:685–696. https://doi.org/10.1085/jgp.200409047

Sack, J.T., N. Stephanopoulos, D.C. Austin, M.B. Francis, and J.S. Trimmer. 2013. Antibody-guided photoablation of voltage-gated potassium currents. *J. Gen. Physiol.* 142:315–324. https://doi.org/10.1085/jgp.201311023

Schmalhofer, W.A., J. Calhoun, R. Burrows, T. Bailey, M.G. Kohler, A.B. Weinglass, G.J. Kaczorowski, M.L. Garcia, M. Koltzenburg, and B.T. Priest. 2008. ProTx-II, a selective inhibitor of NaV1.7 sodium channels, blocks action potential propagation in nociceptors. *Mol. Pharmacol.* 74:1476–1484. https://doi.org/10.1124/mol.108.047670

Schneider, M.F., and W.K. Chandler. 1973. Voltage dependent charge movement of skeletal muscle: a possible step in excitation-contraction coupling. *Nature.* 242:244–246. https://doi.org/10.1038/242244a0

Schneider, C.A., W.S. Rasband, and K.W. Eliceiri. 2012. NIH Image to ImageJ: 25 years of image analysis. *Nat. Methods.* 9:671–675. https://doi.org/10.1038/nmeth.2089

Scholle, A., S. Dugarmaa, T. Zimmer, M. Leonhardt, R. Koopmann, B. Engeland, O. Pongs, and K. Benndorf. 2004. Rate-limiting reactions determining different activation kinetics of Kv1.2 and Kv2.1 channels. *J. Membr. Biol.* 198:103–112. https://doi.org/10.1007/s00232-004-0664-0

Seoh, S.A., D. Sigg, D.M. Papazian, and F. Bezanilla. 1996. Voltage-sensing residues in the S2 and S4 segments of the Shaker K^+ channel. *Neuron.* 16:1159–1167. https://doi.org/10.1016/S0896-6273(00)80142-7

Shibata, R., H. Misonou, C.R. Campomanes, A.E. Anderson, L.A. Schrader, L.C. Doliveira, K.I. Carroll, J.D. Sweatt, K.J. Rhodes, and J.S. Trimmer. 2003. A fundamental role for KChIPs in determining the molecular properties and trafficking of Kv4.2 potassium channels. *J. Biol. Chem.* 278:36445–36454. https://doi.org/10.1074/jbc.M306142200

Singer-Lahat, D., A. Sheinin, D. Chikvashvili, S. Tsuk, D. Greitzer, R. Friedrich, L. Feinshreiber, U. Ashery, M. Benveniste, E.S. Levitan, and I. Lotan. 2007. K^+ channel facilitation of exocytosis by dynamic interaction with syntaxin. *J. Neurosci.* 27:1651–1658. https://doi.org/10.1523/JNEUROSCI.4006-06.2007

Speca, D.J., G. Ogata, D. Mandikian, H.I. Bishop, S.W. Wiler, K. Eum, H.J. Wenzel, E.T. Doisy, L. Matt, K.L. Campi, et al. 2014. Deletion of the Kv2.1 delayed rectifier potassium channel leads to neuronal and behavioral hyperexcitability. *Genes Brain Behav.* 13:394–408. https://doi.org/10.1111/gbb.12120

Stewart, R., B.E. Cohen, and J.T. Sack. 2021. Fluorescent toxins as ion channel activity sensors. *Methods Enzymol.* 653:295–318. https://doi.org/10.1016/bs.mie.2021.02.014

Stoppini, L., P.A. Buchs, and D. Muller. 1991. A simple method for organotypic cultures of nervous tissue. *J. Neurosci. Methods.* 37:173–182. https://doi.org/10.1016/0165-0270(91)90128-M

Swartz, K.J. 2007. Tarantula toxins interacting with voltage sensors in potassium channels. *Toxicon.* 49:213–230. https://doi.org/10.1016/j.toxicon.2006.09.024

Tanabe, T., K.G. Beam, J.A. Powell, and S. Numa. 1988. Restoration of excitation-contraction coupling and slow calcium current in dysgenic muscle by dihydropyridine receptor complementary DNA. *Nature.* 336:134–139. https://doi.org/10.1038/336134a0

Tao, X., A. Lee, W. Limapichat, D.A. Dougherty, and R. MacKinnon. 2010. A gating charge transfer center in voltage sensors. *Science.* 328:67–73. https://doi.org/10.1126/science.1185954

Tilley, D.C., K.S. Eum, S. Fletcher-Taylor, D.C. Austin, C. Dupré, L.A. Patrón, R.L. Garcia, K. Lam, V. Yarov-Yarovoy, B.E. Cohen, and J.T. Sack. 2014. Chemoselective tarantula toxins report voltage activation of wild-type ion channels in live cells. *Proc. Natl. Acad. Sci. USA.* 111:E4789–E4796. https://doi.org/10.1073/pnas.1406876111

Tilley, D.C., J.M. Angueyra, K.S. Eum, H. Kim, L.H. Chao, A.W. Peng, and J.T. Sack. 2019. The tarantula toxin GxTx detains K^+ channel gating charges in their resting conformation. *J. Gen. Physiol.* 151:292–315. https://doi.org/10.1085/jgp.201812213

Trapani, J.G., and S.J. Korn. 2003. Control of ion channel expression for patch clamp recordings using an inducible expression system in mammalian cell lines. *BMC Neurosci.* 4:15. https://doi.org/10.1186/1471-2202-4-15

Tsvetanova, N.G., R. Irannejad, and M. von Zastrow. 2015. G protein-coupled receptor (GPCR) signaling via heterotrimeric G proteins from endosomes. *J. Biol. Chem.* 290:6689–6696. https://doi.org/10.1074/jbc.R114.617951

Turner, M., D.E. Anderson, P. Bartels, M. Nieves-Cintron, A.M. Coleman, P.B. Henderson, K.N.M. Man, P.Y. Tseng, V. Yarov-Yarovoy, D.M. Bers, et al. 2020. α-Actinin-1 promotes activity of the L-type Ca^{2+} channel Ca_v 1.2. *EMBO J.* 39:e102622. https://doi.org/10.15252/embj.2020106171

Vacher, H., D.P. Mohapatra, and J.S. Trimmer. 2008. Localization and targeting of voltage-dependent ion channels in mammalian central neurons. *Physiol. Rev.* 88:1407–1447. https://doi.org/10.1152/physrev.00002.2008

Vierra, N.C., M. Kirmiz, D. van der List, L.F. Santana, and J.S. Trimmer. 2019. Kv2.1 mediates spatial and functional coupling of L-type calcium channels and ryanodine receptors in mammalian neurons. *eLife.* 8:e49953. https://doi.org/10.7554/eLife.49953

Weigel, A.V., P.D. Fox, E.J. Akin, K.H. Ecklund, M.M. Tamkun, and D. Krapf. 2012. Size of cell-surface Kv2.1 domains is governed by growth fluctuations. *Biophys. J.* 103:1727–1734. https://doi.org/10.1016/j.bpj.2012.09.013

Weigel, A.V., M.M. Tamkun, and D. Krapf. 2013. Quantifying the dynamic interactions between a clathrin-coated pit and cargo molecules. *Proc. Natl. Acad. Sci. USA.* 110:E4591–E4600. https://doi.org/10.1073/pnas.1315202110

Woods, G., and K. Zito. 2008. Preparation of gene gun bullets and biolistic transfection of neurons in slice culture. *J. Vis. Exp.* 12:675. https://doi.org/10.3791/675

Xu, H., T. Li, A. Rohou, C.P. Arthur, F. Tzakoniati, E. Wong, A. Estevez, C. Kugel, Y. Franke, J. Chen, et al. 2019. Structural basis of Nav1.7 inhibition by a gating-modifier spider toxin. *Cell.* 176:1238–1239. https://doi.org/10.1016/j.cell.2019.01.047

Yang, W., and R. Yuste. 2017. In vivo imaging of neural activity. *Nat. Methods.* 14:349–359. https://doi.org/10.1038/nmeth.4230

Zagotta, W.N., T. Hoshi, J. Dittman, and R.W. Aldrich. 1994. Shaker potassium channel gating. II: Transitions in the activation pathway. *J. Gen. Physiol.* 103:279–319. https://doi.org/10.1085/jgp.103.2.279

Zhang, G., S. Zheng, H. Liu, and P.R. Chen. 2015. Illuminating biological processes through site-specific protein labeling. *Chem. Soc. Rev.* 44:3405–3417. https://doi.org/10.1039/C4CS00393D

Zhang, A.H., G. Sharma, E.A.B. Undheim, X. Jia, and M. Mobli. 2018. A complicated complex: Ion channels, voltage sensing, cell membranes and peptide inhibitors. *Neurosci. Lett.* 679:35–47. https://doi.org/10.1016/j.neulet.2018.04.030

Zito, K., G. Knott, G.M. Shepherd, S. Shenolikar, and K. Svoboda. 2004. Induction of spine growth and synapse formation by regulation of the spine actin cytoskeleton. *Neuron.* 44:321–334. https://doi.org/10.1016/j.neuron.2004.09.022

Supplemental material

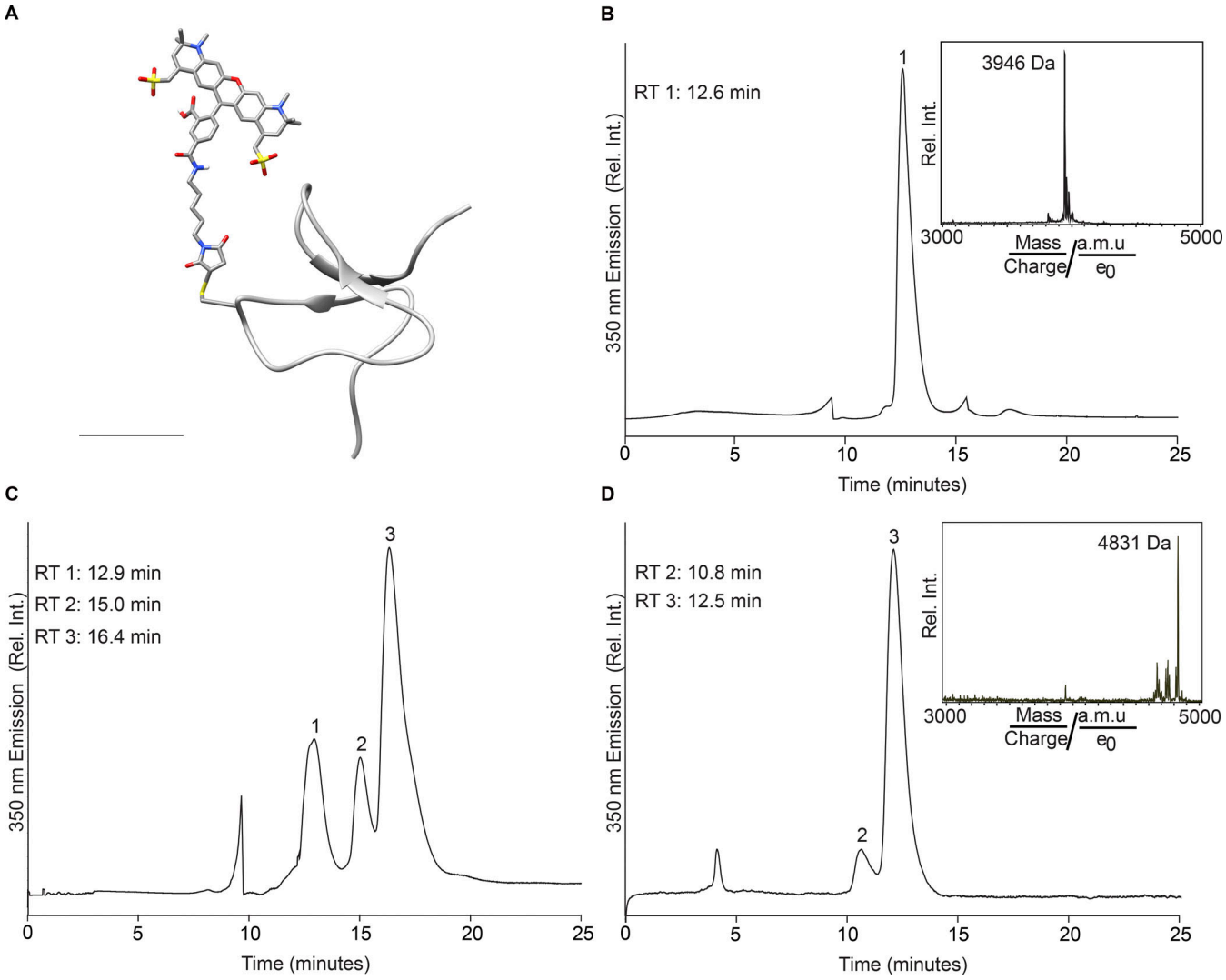

Figure S1. **Synthesis of GxTX-594. (A)** Molecular model of GxTX-594. Scale bar, 10 Å. Backbone of GxTX peptide depicted with ribbon. Cys13(maleimide-Alexa 594) depicted with CPK coloring. **(B)** HPLC chromatogram of Ser13Cys GxTX. Gradient described in –GxTX synthesis. Ser13Cys GxTX eluted at 12.6 min, peak 1, which corresponds to 33% ACN. MALDI-TOF mass spectrometry profile of peak 1 (inset). **(C)** HPLC chromatogram of GxTX-594 conjugation reaction between Alexa Fluor 594-maleimide and Ser13Cys GxTX. Peak 1 is Ser13Cys GxTX (retention time, 12.8 min; 33% ACN); peak 2 is a minor product from conjugation; and peak 3 is GxTX-594, the major product from conjugation (retention time, 16.4 min; 35% ACN). The fractions corresponding to peak 3 were combined. **(D)** HPLC chromatogram of the combined peak 3 fractions from C, a GxTX-594 preparation used in this study. 2 µl of 13.1 µM GxTX-594 diluted in 200 µl of 0.1% TFA was injected. MALDI-TOF mass spectrometry profile of the combined peak 3 fractions (inset). a.m.u., atomic mass unit; Rel. Int., relative intensity.

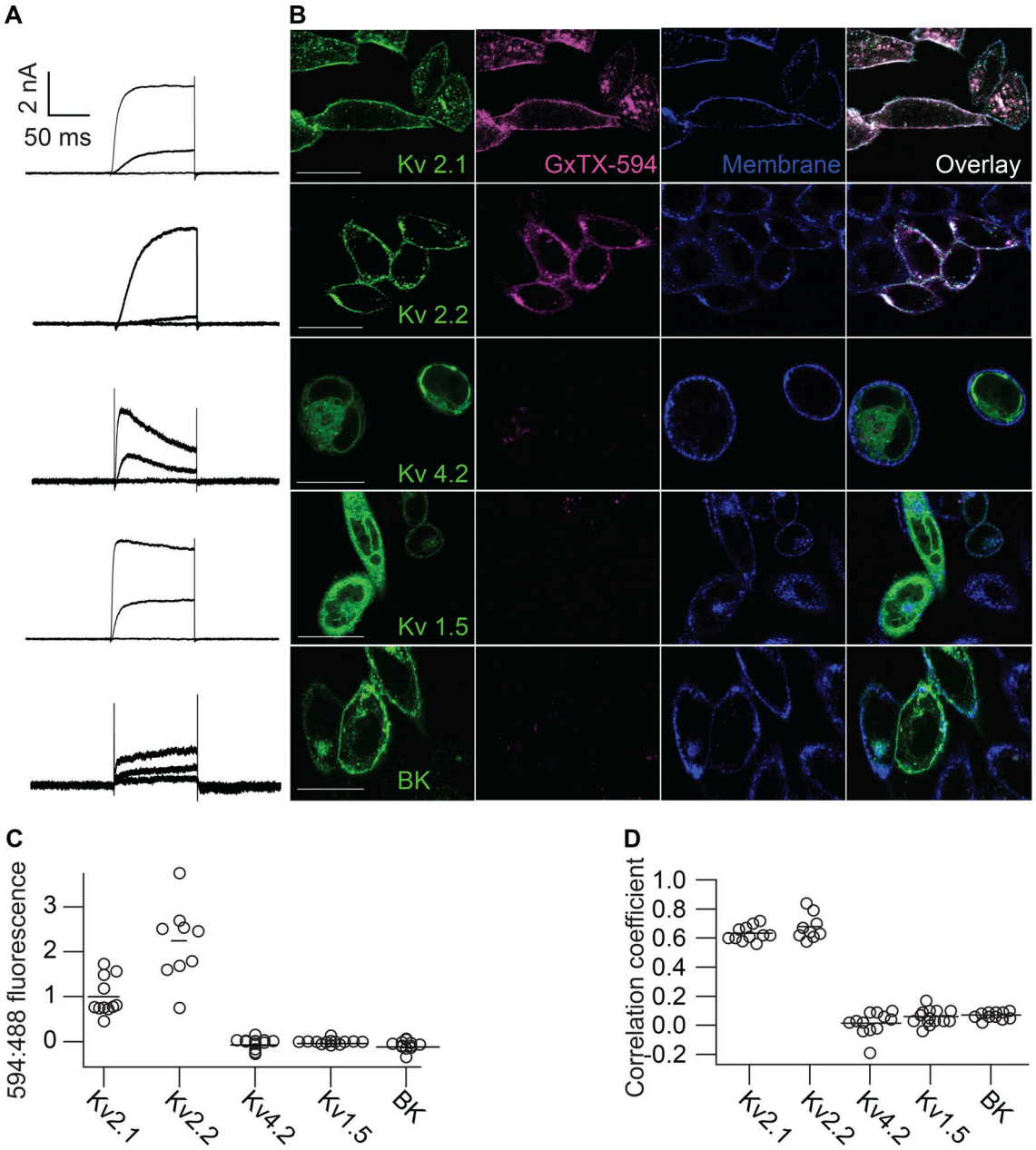

Figure S2. **GxTX-594 selectively labels Kv2 proteins on cell surfaces.** GxTX-594 labeling was assessed in CHO cells expressing Kv2.1-GFP, Kv2.2-GFP, Kv4.2-GFP, Kv1.5-GFP, and BK-GFP. Each of these channel subtypes were assessed for voltage-dependent outward currents to identify cell surface expression of the K^+ channels. CHO cells were not cotransfected with the β subunits for Kv4.2, KChIP2, or Kv1.5, Kvβ2, to assess whether these β subunits interfere with GxTX-594 binding. **(A)** Exemplar whole-cell voltage clamp recordings of CHO cells expressing Kv2.1-GFP, Kv2.2-GFP, Kv4.2-GFP, Kv1.5-GFP, or BK-GFP. Recordings shown are representative responses to 100-ms steps from −100 mV to −40, 0, and +40 mV. **(B)** Confocal imaging of fluorescence from live CHO cells transfected with Kv2.1-GFP, Kv2.2-GFP, Kv4.2-GFP, Kv1.5-GFP, or BK-GFP (indicated by row) and labeled with GxTX-594. Confocal imaging plane was >1 µm above the glass-adhered surface. Cells were incubated with 100 nM GxTX-594 and 5 µg/ml WGA-405 and rinsed before imaging. Fluorescence shown corresponds to emission of GFP (column 1); Alexa Fluor 594 (column 2); WGA-405 (column 3); or an overlay of GFP, Alexa Fluor 594, and WGA-405 (column 4). Scale bars, 20 µm. **(C)** Ratio of fluorescence intensity resulting from excitation of GxTX-594 at 594 nm and GFP at 488 nm. Analysis methods as in Fig. 4 B. Kv2.1, n = 11; Kv2.2, n = 9; Kv4.2, n = 13; Kv1.5, n = 13; and BK, n = 12; n indicates the number of individual cells analyzed in a single dish during a single application of GxTX-594 with the indicated K^+ channel-GFP type. Bars represent the mean. Each circle corresponds to a cell. Significant differences were observed between GxTX:GFP ratio for Kv2.1 or Kv2.2 and Kv1.5, Kv4.2, or BK by Mann–Whitney U test ($P < 0.0001$). The P value to determine significance is adjusted for multiple comparisons using the Bonferroni method, where $P < 0.0033$ is considered significant, with the caveat that data points under each condition are technical replicates. **(D)** Pearson correlation coefficients between GxTX-594 and GFP. Same cells as C. Analysis methods as in Fig. 4 C.

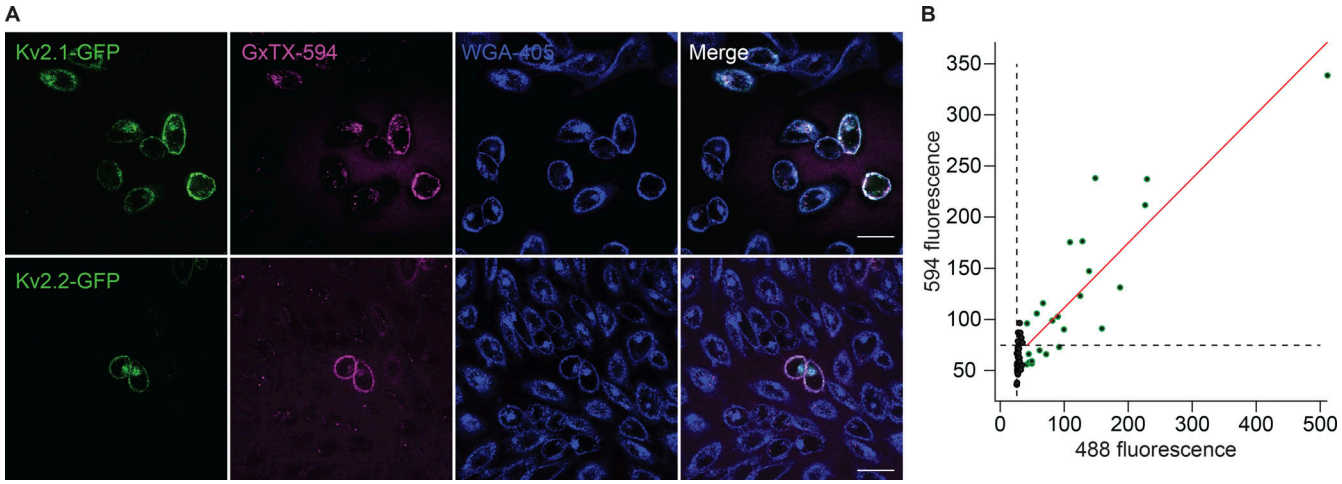

Figure S3. **GxTX-594 labeling of surface membranes requires Kv2 protein.** GxTX-594 partitioning into the membrane was assessed with fluorescence from nontransfected CHO cells and cells transfected with Kv2-GFP proteins. **(A)** Fluorescence from live CHO cells transfected with Kv2.1-GFP (top row) or Kv2.2-GFP (bottom row) and labeled with GxTX-594. Airy disk imaging was at a plane above the glass-adhered surface. Cells were incubated with 100 nM GxTX-594 and 5 µg/ml WGA-405 then diluted to 9 nM GxTX-594 and 0.45 µg/ml WGA-405 before imaging. Scale bars, 20 µm. Fluorescence shown was excited at 488 nm (column 1), 594 nm (column 2), or 405 nm (column 3). Scale bars, 20 µm. **(B)** Fluorescence intensity from Kv2.1-GFP transfected cells with excitation of GxTX-594 at 594 nm versus GFP at 488 nm. Fluorescence from WGA-405 was used as a mask to manually draw ROIs on cells. Each point represents one cell. Cells with obvious GFP fluorescence are green points, cells without are black points. Mean background fluorescence from a region that did not contain cells is indicated by dashed lines. Red line represents a linear fit of cells with obvious GFP fluorescence.

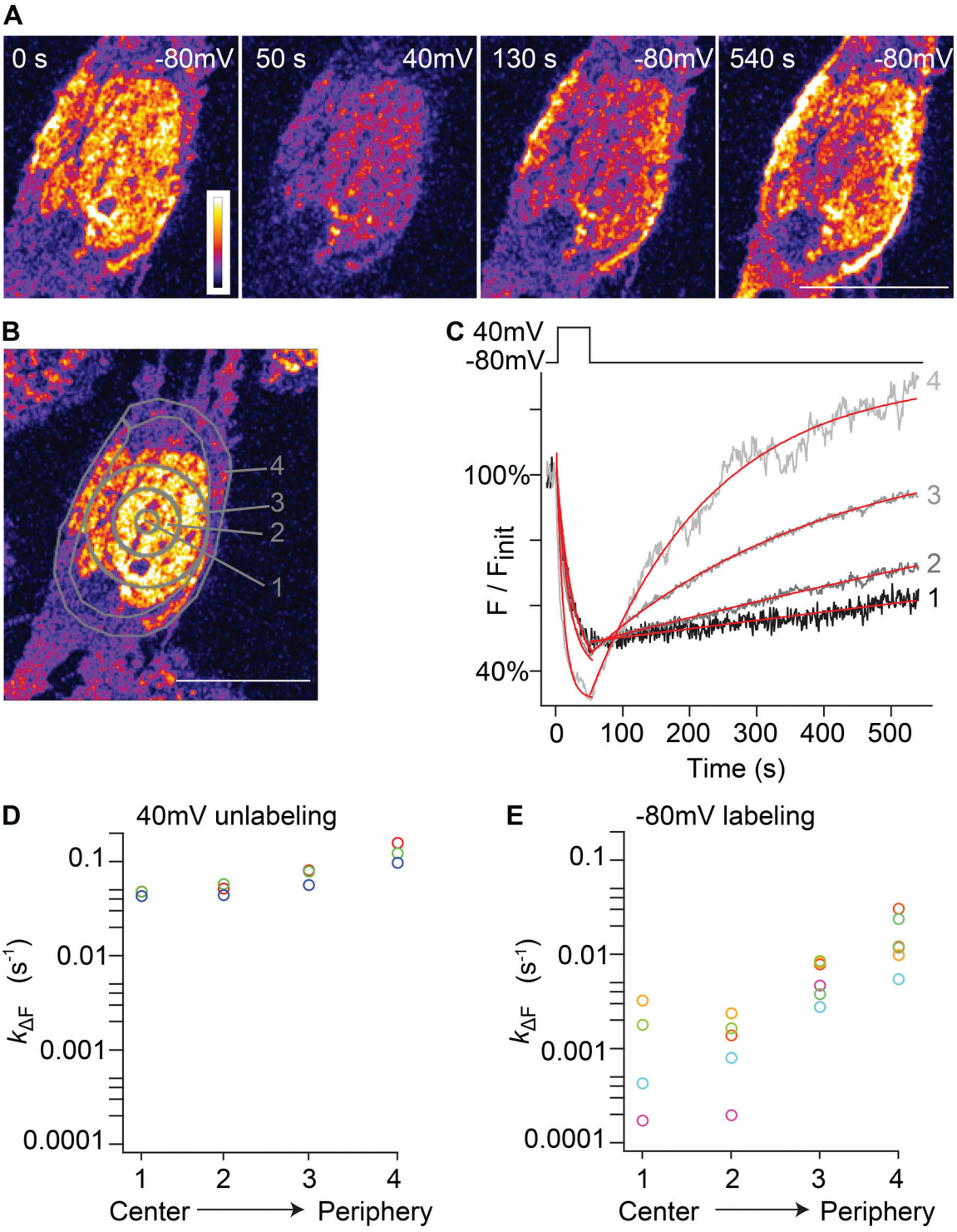

Figure S4. **Extracellular access can impact GxTX-594 labeling kinetics. (A)** Time-lapse Airy disk images of the glass-adhered surface of a voltage-clamped Kv2.1-CHO cell in 9 nM GxTX-594. Time index is in the upper left corner of each panel, and membrane potential is indicated in the upper right corner. Color progression for pseudocoloring of fluorescence intensity is shown in vertical bar on right. Scale bar, 10 µm. **(B)** Airy disk image of the glass-adhered surface of a voltage-clamped Kv2.1-CHO cell in 9 nM GxTX-594. Gray lines indicate boundaries of ROIs. ROIs 1, 2, and 3 are concentric circles, each with a respective diameter of 1.8, 4.9, and 9.1 µm. ROI 4 was hand-drawn to contain the apparent cell surface. In all cells analyzed, ROIs 1–3 were concentric circles of the same sizes, while ROI 4 varied based on cell shape. Scale bar, 10 µm. **(C)** Representative traces of GxTX-594 intensity response to voltage changes. Red lines are monoexponential fits (Eq. 1): 40-mV step ROI 1, $k_{\Delta F}$ = 4.29 × 10^{-2} ± 0.26 × 10^{-2} s^{-1}; ROI 2, $k_{\Delta F}$ = 4.39 × 10^{-2} ± 0.16 × 10^{-2} s^{-1}; ROI 3, $k_{\Delta F}$ = 5.65 × 10^{-2} ± 0.15 × 10^{-2} s^{-1}; and ROI 4, $k_{\Delta F}$ = 9.69 × 10^{-2} ± 0.33 × 10^{-2} s^{-1}. −80-mV step ROI 1, $k_{\Delta F}$ = 4.27 × 10^{-4} ± 0.11 × 10^{-4} s^{-1}; ROI 2, $k_{\Delta F}$ = 7.999 × 10^{-4} ± 0.053 × 10^{-4} s^{-1}; ROI 3, $k_{\Delta F}$ = 2.7556 × 10^{-3} ± 0.0074 × 10^{-3} s^{-1}; and ROI 4, $k_{\Delta F}$ = 5.46 × 10^{-3} ± 0.13 × 10^{-3} s^{-1}. Background for subtraction was the average intensity of a region that did not contain cells over the time course of the voltage protocol. Each trace was normalized to initial fluorescence intensity before the application of the voltage stimulus. **(D)** $k_{\Delta F}$ at +40 mV from individual cells. **(E)** $k_{\Delta F}$ at −80 mV from individual cells. Circle coloring in D and E indicates data from the same cell.

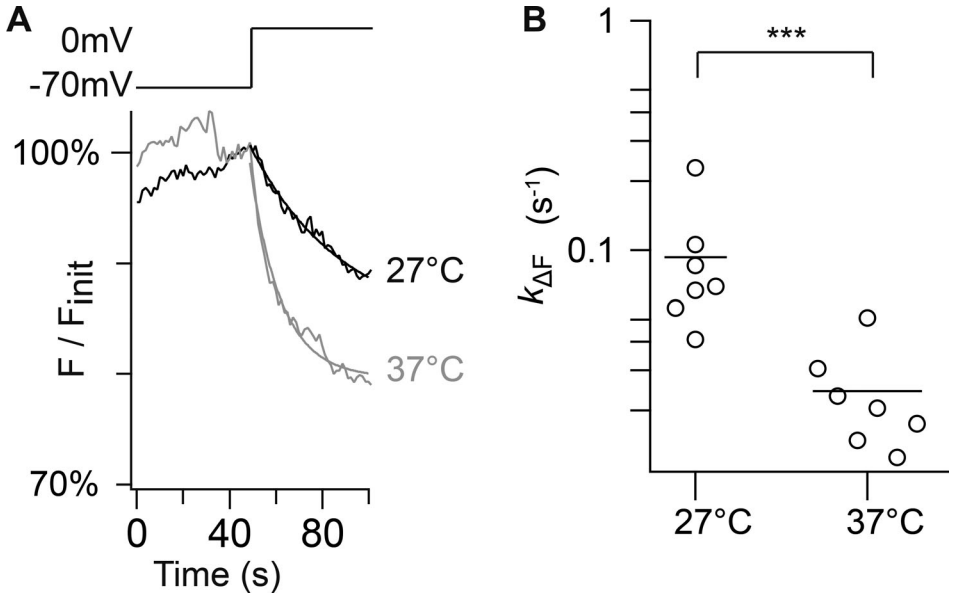

Figure S5. **Variation in temperature does not account for cell-to-cell variability of GxTX-594 kinetics.** Temperature dependence of GxTX-594 labeling was assessed by holding the cell bath solution at either 27°C or 37°C and stepping the membrane voltage from −80 mV to 0 mV for a measurement of $k_{\Delta F}$ at both temperatures. **(A)** Representative traces of GxTX-594 fluorescence intensity response to voltage changes at 27°C (black) and 37°C (gray). Smooth lines are fits of a monoexponential function (Eq. 1): 27°C, $k_{\Delta F}$ = 2.47 × 10^{-2} ± 0.39 × 10^{-2} s^{-1}; 37°C, $k_{\Delta F}$ = 7.54 × 10^{-2} ± 0.54 × 10^{-2} s^{-1}. Background subtraction was performed as in Fig. 6 B. **(B)** $k_{\Delta F}$ at 27°C and 37°C. The rate of fluorescence change was significantly faster at higher temperatures (Mann–Whitney P = 0.0005). From geometric means (bars), a Q_{10} of 3.8 was calculated between 27°C and 37°C. Each circle represents one cell, n = 7 both groups. ***, P < 0.0001.

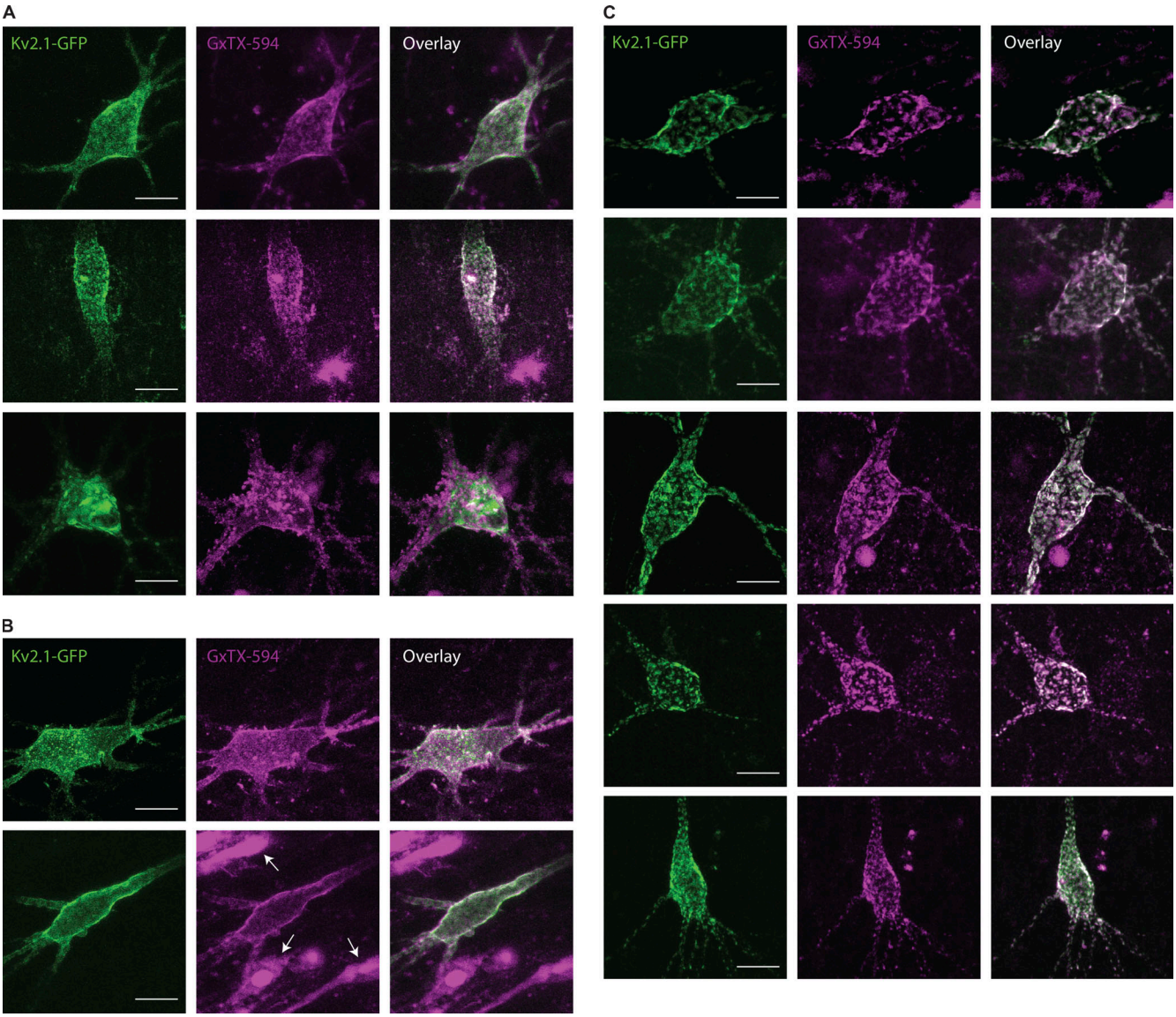

Figure S6. **GxTX-594 labels CA1 hippocampal pyramidal neurons transfected with Kv2.1-GFP.** Two-photon excitation images of rat CA1 hippocampal pyramidal neurons in brain slices as in Fig. 9 A. Kv2.1-GFP (left), GxTX-594 (middle), and overlay (right). Scale bars, 10 µm in all panels. **(A)** Pyramidal neurons 2 d after transfection with Kv2.1-GFP. **(B)** Pyramidal neurons 4 d after transfection with Kv2.1-GFP. **(C)** Pyramidal neurons 6 d after transfection with Kv2.1-GFP.

Video 1. **Time-lapse image sequence of GxTX-594 fluorescence on a voltage-clamped CA1 hippocampal pyramidal neuron while it is depolarized from −70 to 0 mV.** Frame rate, 0.1 fps. Playback speed, 7 fps.

Data S1 is provided online as a separate Excel file and shows a spreadsheet containing model calculations that can be used to generate model prediction.